



Near-infrared and Optical Observations of Type Ic SN 2020oi and Broad-lined Type Ic SN 2020bvc: Carbon Monoxide, Dust, and High-velocity Supernova Ejecta

J. Rho¹ , A. Evans² , T. R. Geballe³ , D. P. K. Banerjee⁴, P. Hoefflich⁵ , M. Shahbandeh⁵ , S. Valenti⁶ , S.-C. Yoon⁷ , H. Jin⁷, M. Williamson⁸ , M. Modjaz⁸ , D. Hiramatsu^{9,10} , D. A. Howell^{9,10}, C. Pellegrino^{9,10} , J. Vinko^{11,12,13} , R. Cartier¹⁴, J. Burke^{9,10}, C. McCully^{9,10} , H. An¹⁵, H. Cha¹⁵, T. Pritchard⁸ , X. Wang^{16,17}, J. Andrews¹⁸ , L. Galbany¹⁹ , S. Van Dyk²⁰ , M. L. Graham²¹ , S. Blinnikov²² , V. Joshi⁴ , A. Pál^{11,13,23} , L. Kriskovics^{11,13}, A. Ordasi¹¹, R. Szakats¹¹ , K. Vida^{11,13} , Z. Chen¹⁶, X. Li¹⁶, J. Zhang²⁴, and S. Yan¹⁶

¹ SETI Institute, 189 Bernardo Avenue, Suite 200, Mountain View, CA 94043, USA; jrho@seti.org

² Astrophysics Group, Keele University, Keele, Staffordshire, ST5 5BG, UK; a.evans@keele.ac.uk

³ Gemini Observatory/NSF's National Optical-Infrared Astronomy Research Laboratory, 670 N. Aohoku Place, Hilo, HI, 96720, USA; tom.geballe@noirlab.edu

⁴ Physical Research Laboratory, Navrangpura, Ahmedabad, Gujarat 380009, India

⁵ Florida State University, Tallahassee, FL 32309, USA

⁶ Department of Physics, University of California, Davis, CA 95616, USA

⁷ Department of Physics and Astronomy, Seoul National University, Gwanak-ro 1, Gwanak-gu, Seoul, 08826, Republic of Korea

⁸ Center for Cosmology and Particle Physics, New York University, 726 Broadway, NY 11201, USA

⁹ Las Cumbres Observatory, 6740 Cortona Drive, Suite 102, Goleta, CA 93117-5575, USA

¹⁰ Department of Physics, University of California, Santa Barbara, CA 93106-9530, USA

¹¹ CSFK Konkoly Observatory, Konkoly-Thege M. ut 15-17, Budapest, 1121, Hungary

¹² Department of Optics and Quantum Electronics, University of Szeged, Dóm tér 9, Szeged, 6720 Hungary

¹³ ELTE Eötvös Loránd University, Institute of Physics, Pázmány Péter sétány 1/A, Budapest, 1117, Hungary

¹⁴ CTIO, NSF's National Optical-Infrared Astronomy Research Laboratory, Casilla 603, La Serena, Chile

¹⁵ Department of Astronomy and Space Science, Chungbuk National University, Cheongju, 28644, Republic of Korea

¹⁶ Physics Department, Tsinghua University, Beijing, 100084, People's Republic of China

¹⁷ Beijing Planetarium, Beijing Academy of Science and Technology, Beijing, 100089, People's Republic of China

¹⁸ Steward Observatory, University of Arizona, 933 North Cherry Avenue, Tucson, AZ 85721, USA

¹⁹ Departamento de Física Teórica y del Cosmos, Universidad de Granada, E-18071 Granada, Spain

²⁰ Caltech/IPAC, Mailcode 100-22, Pasadena, CA 91125, USA

²¹ DiRAC Institute, Department of Astronomy, University of Washington, Box 351580, U.W., Seattle WA 98195, USA

²² NRC Kurchatov Institute—IITEP, Moscow, 117218; Sternberg Astronomical Institute (SAI) of Lomonosov Moscow State University, Moscow, 117218; Dukhov Automatics Research Institute (VNIIA), Moscow, 127055, Russia

²³ ELTE Eötvös Loránd University, Department of Astronomy, Pázmány Péter sétány 1/A, Budapest, 1117, Hungary

²⁴ Yunnan Observatories, Chinese Academy of Sciences, Kunming, 650216, People's Republic of China

Received 2020 August 15; revised 2020 December 24; accepted 2020 December 29; published 2021 February 25

Abstract

We present near-IR (NIR) and optical observations of the Type Ic supernova (SN Ic) SN 2020oi in the galaxy M100 and the broad-lined SN Ic SN 2020bvc in UGC 9379, using Gemini, Las Cumbres Observatory, Southern Astrophysical Telescope, and other ground-based telescopes. The NIR spectrum of SN 2020oi at day 63 since the explosion shows strong CO emissions and a rising K -band continuum, which is the first unambiguous dust detection from an SN Ic. Non-LTE CO modeling shows that CO is still optically thick and that the lower limit to the CO mass is $10^{-3} M_{\odot}$. The dust temperature is 810 K, and the dust mass is $\sim 10^{-5} M_{\odot}$. We explore the possibilities that the dust is freshly formed in the ejecta, heated dust in the preexisting circumstellar medium, and an infrared echo. The light curves of SN 2020oi are consistent with a STELLA model with canonical explosion energy, $0.07 M_{\odot}$ Ni mass, and $0.7 M_{\odot}$ ejecta mass. A model of high explosion energy of 10^{52} erg, $0.4 M_{\odot}$ Ni mass, and $6.5 M_{\odot}$ ejecta mass with the circumstellar matter reproduces the double-peaked light curves of SN 2020bvc. We observe temporal changes of absorption features of the IR Ca II triplet, Si I at $1.043 \mu\text{m}$, and Fe II at 5169 \AA . The blueshifted lines indicate high velocities, up to $60,000 \text{ km s}^{-1}$ for SN 2020bvc and $20,000 \text{ km s}^{-1}$ for SN 2020oi, and the expansion velocity rapidly declines before the optical maximum. We present modeled spectral signatures and diagnostics of CO and SiO molecular bands between 1.4 and $10 \mu\text{m}$.

Unified Astronomy Thesaurus concepts: Core-collapse supernovae (304); Type Ic supernovae (1730); Carbonaceous grains (201); Cosmochemistry (331); Interstellar molecules (849); Molecular spectroscopy (2095); High resolution spectroscopy (2096); Line intensities (2084); Silicate grains (1456); Interstellar dust (836); Explosive nucleosynthesis (503); Nucleosynthesis (1131)

Supporting material: data behind figures

1. Introduction

The large amount of dust seen in high- z galaxies implies that dust forms in the early universe (Isaak et al. 2002; Bertoldi et al. 2003; Laporte et al. 2017). Intermediate-mass stars, thought to produce most interstellar dust in present galaxies, when they are in the AGB phase, would not have evolved to

the dust-producing stage in high- z galaxies because the universe was too young (Michałowski 2015; Leńniewska & Michałowski 2019). In contrast, core-collapse supernovae (CCSNe) can occur just several million years after their progenitors form, offering an explanation for the source of dust early in the universe. The mapping of the young SN remnant

(SNR) Cas A confirmed that dust and carbon monoxide (CO) form in SN ejecta (Rho et al. 2008, 2012). Several SNRs, namely, Cas A (De Looze et al. 2017), SN 1987A (Matsuura et al. 2015), G54.1+0.3 (Rho et al. 2018b), the Crab Nebula (Gomez et al. 2012), and three additional pulsar wind nebula SNRs (Chawner et al. 2019), have dust masses of 0.1–0.9 M_{\odot} , in agreement with dust formation models (Todini & Ferrara 2001; Nozawa et al. 2003; Sluder et al. 2018). These results suggest that CCSNe are viable major dust factories in the early universe. However, understanding of the amount of dust destruction by reverse shocks in the SN ejecta is a subject of debate (Nozawa et al. 2007; Nath et al. 2008; Silvia et al. 2010; Micelotta et al. 2016; Kirchschrager et al. 2019). Estimates from a number of studies of the dust mass per SN event in recent SNe are more than two orders of magnitude lower (e.g., Kotak et al. 2009; Andrews et al. 2011) than the masses measured in the young SNRs mentioned above.

SNe from core collapse are classified as Type II if they exhibit H lines, as Type Ib if they exhibit He lines but no H lines, and as Type Ic if they do not exhibit either H or He lines (e.g., Filippenko 1997; Gal-Yam 2017; Williamson et al. 2019). The latter types likely arise from progenitors that have lost their hydrogen envelopes (for SNe Ib) and also most, if not all, of their helium envelopes (for SNe Ic). SNe Ib and Ic are usually referred to as stripped-envelope CCSNe.

The spectra of an SN Ic subgroup, SNe Ic-BL, are characterized by broad lines (BLs) implying very high velocities ($>20,000$ km s^{-1} at maximum light; Modjaz et al. 2016), which, for some objects, may indicate higher explosion energies ($\sim 10^{52}$ erg) than for typical SNe Ic. SNe Ic-BL are of great interest because they are the only type of SN associated with γ -ray bursts (GRBs; see reviews by, e.g., Woosley & Bloom 2006; Modjaz 2011; Cano et al. 2017). There is considerable controversy over “hidden” He (e.g., Dessart et al. 2011; Hachinger et al. 2012), especially regarding whether the lack of obvious optical He lines in SN Ic and SN Ic-BL spectra is evidence for helium deficiency in the ejecta. This controversy applies to the entire SN Ic family, including SN-GRBs and superluminous SN Ic (Mazzali et al. 2016). The apparent lack of He in SN Ic and SN Ic-BL spectra is puzzling since most of the progenitors of SNe Ic-BL and GRBs are He stars (Fryer et al. 2007; Yoon 2015). Answering the He question is crucial for understanding the stellar progenitors of SNe Ic and SNe Ic-BL (Yoon 2017), including those connected with GRBs. Near-IR (NIR) spectra are crucial for determining the presence of He and for identifying the stellar progenitors of SNe Ic (Dessart et al. 2012, 2015).

We recently obtained a sequence of NIR spectra of the Type IIP CCSN SN 2017eaw, which shows the onset of CO formation and newly formed carbon dust (Rho et al. 2018a; Szalai et al. 2019; Tinyanont et al. 2019). The timing of the appearance and the evolution of CO is remarkably similar to that seen in SN 1987A and is consistent with chemically controlled dust models. Some dust formation models (Todini & Ferrara 2001; Nozawa et al. 2003) predict that dust forms between 350 and 900 days after the explosion, with carbon dust being one of the first condensates. The dust mass produced in SN ejecta depends on progenitor mass and on the SN type (Todini & Ferrara 2001; Sarangi & Cherchneff 2013).

In this paper we present Gemini-GNIRS NIR target-of-opportunity spectroscopy of two CCSNe, the Type Ic SN 2020oi and the Type Ic-BL SN 2020bvc, together with NIR

spectroscopy from the Southern Astrophysical Telescope (SOAR) and IRTF, optical spectroscopy and photometry from the Las Cumbres Observatory (LCO) network, and other ground-based telescopes. The two SNe discovered within days of the explosion were rapidly observed and classified as described below. Here we present and analyze the early data from day 1 to ~ 100 after the explosions.

2. Observations

SN 2020oi (ZTF20aaelulu) was discovered on 2020 January 7 by the Zwicky Transient Facility (ZTF) at $r = 17.28$ mag (TNS 51926; Forster et al. 2020). It is located in the nearby galaxy M100 at a distance of 16.22 Mpc based on NED²⁵ with $z = 0.00524$. Based on an optical spectrum obtained at the SOAR, it was classified as Type Ic (ATel # 13393; Siebert et al. 2020). The SN has also been detected by Swift with UVW2 = 17.97 ± 0.33 , UVM2 = 18.16 ± 0.34 , and UVW1 = 17.54 ± 0.25 (TNS 2020-8; Ho et al. 2020d). In addition, radio emission has been reported (ATel # 13398, 13400, 13401, and 13448; Horesh et al. 2020; Moldon et al. 2020).

SN 2020bvc was discovered by the All Sky Automated Survey for Supernovae (ASAS-SN) on 2020 February 4 at g magnitude ~ 17 (Stanek 2020). It is located in the galaxy UGC 09379, at a distance of 114 Mpc, with $z = 0.025235$ based on NED. SN 2020bvc was classified as a young CCSN based on optical spectra from LCO by Hiramatsu et al. (2020). It was further classified as a broad-lined SN Ic by Perley et al. (2020). Early ZTF, LT, and ASAS-SN photometry show it to have had an extremely rapid initial rise, followed by a rapid decline (Perley et al. 2020). Radio emission has been detected by the Very Large Array, and X-ray emission has been detected by Chandra (Ho et al. 2020b). No counterpart GRB to SN 2020bvc has been detected. It has been suggested by Izzo et al. (2020) that the lack of a counterpart GRB is due to it being an off-axis GRB or having a choked jet. Ho et al. (2020c) present double-peaked light curves of SN 2020bvc.

NIR 0.8–2.5 μm spectra of SN 2020oi and SN 2020bvc were obtained by the Gemini Near-Infrared Spectrograph (GNIRS) on the 8.1 m Frederick C. Gillett Gemini-North telescope, for program GN-2020A-Q-211. The observing dates are listed in Table 1. GNIRS was configured in its cross-dispersed mode, using its 32 line mm^{-1} grating and a $0''.45$ -wide slit to provide a resolving power, R , of ~ 1200 (250 km s^{-1}) for the first spectrum of SN 2020oi and the SN 2020bvc spectrum and a $0''.675$ -wide slit to nominally provide $R = 800$ (375 km s^{-1}) for the second SN 2020oi spectrum (the seeing was much better than $0''.675$). The observational setup and data reduction procedures were the same as those used for SN 2017eaw as described in Rho et al. (2018a). The spectra shown here have been binned such that the separation of adjacent data points, $\Delta\lambda$, corresponds to $\lambda/\Delta\lambda \sim 1000$. Due to the COVID-19 pandemic, Gemini-North telescope was closed from 2020 March 22. After Gemini-North reopened, we obtained a GNIRS spectrum at the position of SN 2020oi on 2020 May 31, but the SN was not detected.

NIR spectra of SN 2020oi were obtained with TripleSpec v4.1, the fourth generation of the TripleSpec instrument mounted on the NIR Nasmyth port of the 4.1 m SOAR

²⁵ <http://ned.ipac.caltech.edu/>

Table 1
Observational Parameters of Optical and Infrared Spectroscopy

No.	Date	MJD	Day	Instrument
SN 2020oi				
No. ^a	20200106	58854.04	0(= t_0) ^b	...
1	20200108	58856	2	SOAR-Goodman
101	20200109^c	58857	3	SOAR-TripleSpec
2	20200109	58857	3	SOAR-Goodman
3	20200111	58859	5	Lijiang-YFOSC
4	20200117	58865	11	Xinglong-BFOSC
5	20200118	58867	12	SOAR-Goodman
6	20200120	58868	14	Xinglong-BFOSC
102	20200120^c	58869	14	IRTF-SPEX
7	20200121	58869	15	LCOFTN-FLOYDS
8	20200131	58879	25	LCOFTN-FLOYDS
103	20200204^c	58884	29	Gemini-GNIRS
9	20200205	58884	30	LCOFTN-FLOYDS
10	20200211	58890	36	SOAR-Goodman
11	20200215	58894	40	Bok-BCspec
12	20200218	58897	43	Xinglong-BFOSC
104	20200309^c	58917	63	Gemini-GNIRS
13	20200313	58921	67	Xinglong-BFOSC
SN 2020bvc				
	20200203	58882.67	0(= t_0) ^d	...
1	20200205	58884	1.33	LCOFTN-FLOYDS
2	20200215	58894	10	Bok-BCSpec
3	20200224	58903	20	LCOFTN-FLOYDS
4	20200225	58904	21	APO3.5m-DIS
101	20200306^c	58914	31	Gemini-GNIRS
5	20200321	58929	46	LCOFTN-FLOYDS
6	20200323	58931	48	LCOFTN-FLOYDS
7	20200402	58941	58	LCOFTN-FLOYDS
8	20200417	58956	73	LCOFTN-FLOYDS

Notes.

^a The number of observations counting optical spectroscopy starts from 1 and NIR starts from 101 for SN 2020oi and SN 2020bvc, respectively.

^b The explosion date of SN 2020oi is estimated to be on 2020 January 6 (MJD = 58854), taken to be the middle point between the last nondetection reported by ZTF and the first detection.

^c NIR observations are marked in bold. The GNIRS observations of SN 2020oi on 20200204 approximately have J , H , and K magnitudes of 14.9, 14.5, and 14.3 mag, respectively. The GNIRS observations of SN 2020oi on 20200309 have J , H , and K magnitudes of 16.3, 16.2, and 16.1 mag, respectively. The GNIRS observations of SN 2020bvc on 20200306 have J , H , and K magnitudes of 16.7, 15.7, and 15.6 mag, respectively.

^d The explosion date is from Ho et al. (2020c).

telescope; previous versions of TripleSpec were built for the 200-inch Palomar telescope, the ARC 3.5 m telescope, and the Keck II telescope. TripleSpec is a cross-dispersed spectrograph featuring six spectral orders, spanning 0.8–2.4 μm with a nominal resolution of $R \sim 3500$, composed of a fixed-format slit assembly 1"1 wide and 28" long and a 2048 \times 2048 Hawaii-2RG HgCdTe detector array. TripleSpec at SOAR is fed by a reflection off a dichroic, which also transmits light to the guider. As a result, the response cuts off below 1.0 μm . The nominal point of 50% reflectivity of the dichroic is around 0.95 μm .

We used the Spextool IDL package (Cushing et al. 2004) to reduce the TripleSpec data, and we subtracted consecutive AB pairs to remove the sky and the bias level. We flat-fielded the science frames dividing by the normalized master flat. We calibrated 2D science frames in wavelength by using CuHeAr

Hollow Cathode comparison lamps. To correct for telluric features and to flux-calibrate our SN spectrum, we observed the A0V telluric standard after the SN and at a similar air mass. Finally, we extracted the SN and the telluric star spectra from the 2D wavelength-calibrated frames. After the extraction of the individual spectra, we used the xtellcorr task (Vacca et al. 2003) included in the Spextool IDL package to perform the telluric correction and the flux calibration of the spectra of SN 2020oi.

LCO $UBVgri$ -band data were obtained with the Sinistro camera on the 1 m telescopes at Sutherland (South Africa), CTIO (Chile), Siding Spring (Australia), and McDonald (USA), through the Global Supernova Project. Point-spread function fitting was performed using lcogetsnpipe²⁶ (Valenti et al. 2016), a PyRAF-based photometric reduction pipeline. As SN 2020oi occurred in the same galaxy as SN 2019ehk (Grzegorzec 2019), image subtraction was performed using as templates Sinistro images of SN 2019ehk (taken between 20191201 and 20191207), using PyZOGY (Guevel & Hosseinzadeh 2017), an implementation in Python of the subtraction algorithm described in Zackay & Ofek (2017). UBV -band data were calibrated to Vega magnitudes (Stetson 2000) using standard fields observed on the same night by the same telescope as the SN. gri -band data were calibrated to AB magnitudes using the Sloan Digital Sky Survey (SDSS; SDSS Collaboration 2017).

Additional photometric data were collected with the 0.8 m RC80 telescope of Konkoly Observatory through Johnson BV and Sloan $griz$ filters at Piszkestető station (Hungary). Photometry was performed via image subtraction of PS1²⁷ template frames implemented in IRAF. Photometric zero-points in each filter were tied to PS1 photometry of 5–10 local stars used as tertiary standards. B and V magnitudes of the local standards in the Vega system were derived from their g_P , r_P , and i_P data via the calibration of Tonry et al. (2012), while the magnitudes in the g , r , i , and z filters are given in the AB system. We also added gr -band ZTF (Bellm et al. 2019) photometric data for both SN 2020oi and SN 2020bvc.

LCO optical spectra were taken with the FLOYDS spectrographs mounted on the 2 m Faulkes Telescope North (FTN) and South at Haleakala (USA) and Siding Spring (Australia), respectively, through the Global Supernova Project. A 2" slit was placed on the target at the parallactic angle (Filippenko 1982). One-dimensional spectra were extracted, reduced, and calibrated following standard procedures using the FLOYDS pipeline²⁸ (Valenti et al. 2014). The wiggles in the FLOYDS spectra that appear above 7500 Å are due to fringes.

We also acquired optical spectra with Goodman on the SOAR telescope (Clemens et al. 2004) and the Boller & Chivens spectrograph (BCSpec) on the 2.3 m Bok telescope. In addition, we obtained a low-resolution spectrum with the Dual Imaging Spectrograph (DIS), mounted on the 3.5 m telescope at the Apache Point Observatory. The R300 grating had a central wavelength of 7500 Å. The instrument was rotated to the parallactic angle, and 1 \times 400 s exposures were obtained. These data were reduced using standard procedures and calibrated to a standard star obtained the same night using the PyDIS package (Davenport 2018). Finally, a few optical spectra of SN 2020oi were observed using the Yunnan Faint

²⁶ <https://github.com/svalenti/lcogetsnpipe>

²⁷ <https://ps1images.stsci.edu>

²⁸ https://github.com/svalenti/FLOYDS_pipeline

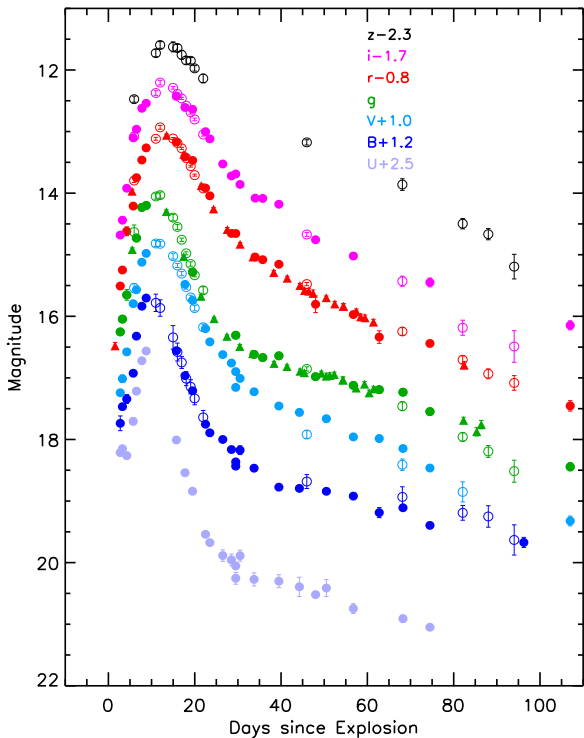


Figure 1. Multicolor light curves of SN 2020oi from LCO (filled circles), Konkoly (open circles), and ZTF (filled triangles). The explosion date of 2020 January 6 (MJD = 58,854), taken to be the middle point between the last nondetection reported by ZTF and the first detection, is used as day 0 (t_0). The magnitudes are shifted as labeled for display purposes.

(The data used to create this figure are available.)

Object Spectrograph and Camera (YFOSC) on the 2.4 m Lijiang optical telescope (LJT; Wang et al. 2019; Xin et al. 2020) and Beijing Faint Object Spectrograph and Camera (BFOSC) on the Xinglong 2.16 m telescope (Fan et al. 2016) of the Beijing Astronomical Observatory (BAO). The observations are summarized in Table 1.

3. Results

3.1. Extinction

We have examined the Na I D lines from the optical spectra of both SNe (see Figure 6) and do not detect distinct doublets but do notice marginal dips at Na I D1 and D2 in some of the spectra of SN 2020oi. We have estimated the Galactic reddening toward the exact direction of the SN 2020oi and SN 2020bvc using the Galactic dust model of Schlafly & Finkbeiner (2011).²⁹ The Galactic reddening is very small, $E(B - V) = 0.0227 \pm 0.0002$, in the direction of the SN 2020oi, and is even smaller, $E(B - V) = 0.0106 \pm 0.0004$, in the direction of SN 2020bvc. The corrections are less than the sizes of the plotting symbols in the figures. The extinctions we derive from marginal dips in SN 2020oi are consistent with the techniques described in Poznanski et al. (2012). The estimated extinction of SN 2020oi is comparable to those of Izzo et al. (2020) and Ho et al. (2020c), and that of SN 2020bvc is comparable to that of Horesh et al. (2020).

3.2. Light Curves and Explosion Properties of SN 2020oi

The light curves of SN 2020oi are shown in Figure 1. SN 2020oi was discovered by the ZTF on 2020 January 7 (MJD = 58855.54)³⁰ at a magnitude of $r = 17.28$, and the last nondetection reported by the ZTF survey is on 2020 January 4 (MJD = 58852.546) to a depth of $r = 20.52$ mag. Assuming that the explosion time occurred at the middle point between the discovery and the last nondetection, SN 2020oi exploded on 2020 January 6 (t_0 ; MJD = 58,854.04 \pm 1.5). The light curves of SN 2020oi show a gradual increase over ~ 10 days, peaking around January ~ 13 –18 (depending on the wavelength), and decreasing rapidly for 25 days. Thereafter the light curves are rather flat or decrease rather more slowly (~ 0.3 mag) over ~ 40 days (~ 0.0075 mag day⁻¹). This behavior is as expected for the ⁵⁶Co to ⁵⁶Fe decay with a slope of 0.0098 mag day⁻¹.

After 65 days, the light curves in the g and V bands show slightly steeper slope, which is common in SNe Ib/Ic. This more rapid decline is indicative of significant γ -ray escape due to the low mass of the ejecta (Clocchiatti & Wheeler 1997; Sollerman et al. 1998). The peak in the light curve in the V band is on 2020 January 17 (MJD_{Vmax} = 58,865.52 \pm 0.14) at $V_{\text{max}} = 13.81 \pm 0.03$ mag, determined using a light-curve peak finder code based on Monte Carlo simulation (Bianco et al. 2014). The peak in the light curve in the B band is on 2020 January 15 (MJD_{Bmax} = 58863.15 \pm 0.20) at $B_{\text{max}} = 14.73 \pm 0.02$ mag. The dates of V_{max} and B_{max} are 11.5 and 9.1 days after t_0 (Figure 1), respectively.

We have compared the observed UBVgriz-band light curves from the LCO network, Konkoly, and ZTF with some SN models, obtained using the one-dimensional multigroup radiation hydrodynamics code STELLA (Blinnikov et al. 2000, 2006). The STELLA code employs a predictor-corrector high-order implicit scheme for line emission and calculates the spectral energy distributions (SEDs) at each time step. The multicolor light curves are obtained by convolving the filter response functions with the SEDs. The STELLA code also implicitly treats time-dependent equations of the angular moments of intensity averaged over a frequency bin with the variable Eddington method until the agreement with hydrodynamics is achieved at each time step.

When a progenitor star loses its envelopes of hydrogen and helium by its interaction with a binary companion, the explosion of the carbon–oxygen (C–O) star is triggered by Fe core collapse and leads to an explosion of Type Ic. Using the model grids in Yoon et al. (2019), we find that the multicolor light curves of SN 2020oi are well reproduced by the SN Ic model “CO2.16_fm5.0_E1.0,” which has an explosion energy of $E_{\text{exp}} = 1.0 \times 10^{51}$ erg and a nickel mass of 0.07 M_{\odot} , as seen in Figure 2. The progenitor of this SN model is a helium-poor C–O star of mass 2.16 M_{\odot} ; the corresponding initial mass of the progenitor is about 13 M_{\odot} . The adopted mass cut (where the SN energy is injected in mass coordinates) is 1.45 M_{\odot} , assumed to be the mass of the neutron star, and the corresponding ejecta mass is 0.71 M_{\odot} . We assume in our model that the mass cut is the outer boundary of the iron core. The nickel is assumed to be fully mixed (see Figure 1 of Yoon et al. 2019, for the Ni distribution of $f_m = 5.0$) in the SN ejecta.

We checked the light-curve fitting and parameter estimates by assembling the bolometric light curve and fitting it with an

²⁹ <https://irsa.ipac.caltech.edu/applications/DUST/>

³⁰ <https://lasair.roe.ac.uk/object/ZTF20aaelulu/>

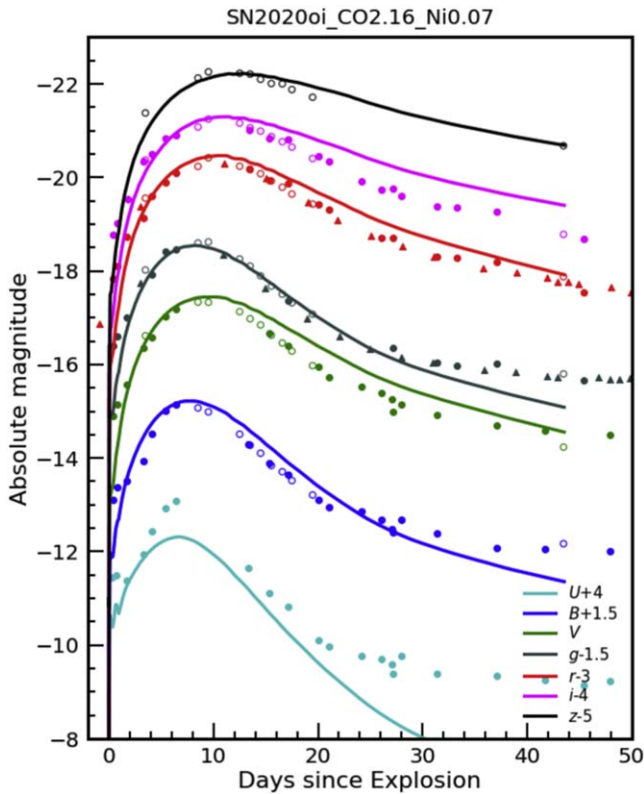


Figure 2. Light curves of SN 2020oi superposed on the SN Ic model from a $2.16 M_{\odot}$ CO star progenitor, with an explosion energy of 1×10^{51} erg and a nickel mass of $0.07 M_{\odot}$.

Arnett model (Arnett 1982; Valenti et al. 2008; Chatzopoulos et al. 2012). This model family assumes homologous expansion of constant-density ejecta, powered by centrally located radioactive ^{56}Ni , and solves the equation of radiation diffusion assuming constant opacity. The fitting resulted in physical parameters that are consistent with the STELLA model fitting above: ejecta mass in between 0.5 and $1.1 M_{\odot}$ (depending on the opacity) and initial ^{56}Ni mass of $0.07 \pm 0.01 M_{\odot}$.

The light curves of SN 2020oi are compared with those of other SNe Ic of SN 2007gr, SN 1994I, and SN 2006jc in Figure 3. The photometry and spectra of other SNe are obtained from the Open SN catalog.³¹ The light curve of SN 2020oi is remarkably similar to that of SN 1994I. The two SNe, SN 2007gr and SN 2006jc, show slower declines after their peaks than SN 2020oi. The progenitor and explosion properties of the three SNe Ic are compared in Table 2. The explosion energy, Ni mass, and ejecta mass ($E_{\text{exp}} \sim 1 \times 10^{51}$ erg, $M_{\text{Ni}} \sim 0.07 M_{\odot}$, and $M_{\text{ej}} \sim 0.71 M_{\odot}$) of SN 2020oi are indeed similar to those of SN 1994I. In contrast, SN 2007gr has a higher ejecta mass. The $2.16 M_{\odot}$ CO star in SN 2020oi can be made via binary interaction. The mass of the circumstellar medium (CSM) could not be tightly constrained from optical curves without detection of the first peak (observed in SN 2020bvc; see Figure 5), but the comparable model in Figure 2 assumes an upper limit to the CSM mass of $3 \times 10^{-4} M_{\odot}$, which is still consistent with the observation. It does not contradict the recent findings based on radio observations by Horesh et al. (2020).

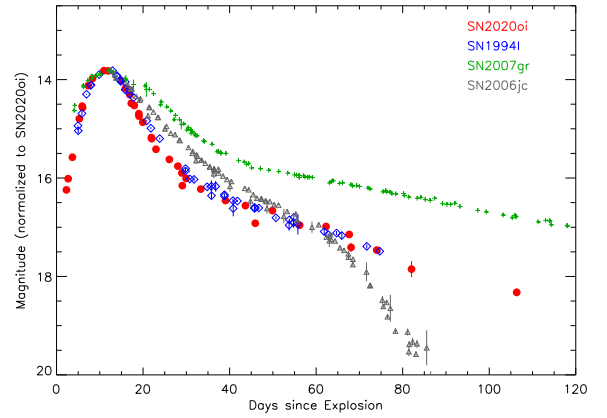


Figure 3. Optical light curve of SN 2020oi in V band compared with those of SN 2007gr, SN 1994I, and SN 2006jc. The light curves of the three SNe are scaled to match that of SN 2020oi at its peak.

3.3. Light Curves and Explosion Properties of SN 2020bvc

Figure 4 shows optical light curves of SN 2020bvc with LCO, Konkoly, and ZTF photometry. We use 2020 February 3.67 (MJD = 58,882.67) from Ho et al. (2020c) as day 0, which is based on the time of the ATLAS nondetection. The maximum in the V-band light curve occurred on 2020 February 20 (MJD $_{V_{\text{max}}} = 58,899 \pm 0.12$) at $V_{\text{max}} = 16.36 \pm 0.02$ mag. The maximum in the B-band light curve occurred on 2020 February 12 (MJD $_{B_{\text{max}}} = 58,891.26 \pm 0.12$) at $B_{\text{max}} = 17.18 \pm 0.01$ mag. The dates of V_{max} and B_{max} are 16.32 and 8.6 days after t_0 (Figure 4), respectively. After reaching maxima, the light curves show gradual decreases until day ~ 100 (the end of the coverage). The peak of SN 2020bvc is shallower than that of SN 2020oi by ~ 1 mag.

To reproduce the light curves of SN 2020bvc, we have calculated a new SN model (based on Yoon et al. 2019) with a helium-poor CO star of mass $8.26 M_{\odot}$, which corresponds to a progenitor of mass $40\text{--}50 M_{\odot}$ (the full grid of models will be published elsewhere). We include the double-peaked light curves from Ho et al. (2020c) for modeling to derive explosion parameters. We convert the light curves from Ho et al. (2020c) in the AB system to the Vega system to compare with our LCO, Konkoly, and simulated light curves. The model is superposed on the light curve of SN 2020bvc in Figure 5. The assumed mass cut is $1.86 M_{\odot}$, and hence the ejecta mass is $6.40 M_{\odot}$. We find that an explosion energy of $E_{\text{exp}} = 12 \times 10^{51}$ erg and a radioactive nickel mass of $0.4 M_{\odot}$ lead to a reasonably good fit for the main peak and the light-curve width (Figure 5). The nickel is assumed to be uniformly mixed in the inner region of the SN ejecta (see Figure 1 of Yoon et al. 2019, for the Ni distribution of $f_m = 0.9$), encompassing 90% of the ejecta mass. If this SN had a magnetar engine (e.g., Kasen & Bildsten 2010), the actual nickel mass would be smaller than our estimate from the model.

The light curves of SN 2020bvc in the optical are double peaked. To explain the first peak, we assume that the progenitor was surrounded by massive CSM having the standard “stellar wind density profile (ρ)” of $\rho = \dot{M}/4\pi v_w r^2$, where \dot{M} is the mass-loss rate, v_w is the wind velocity, and r is the radius of a stellar wind. Within the parameter space we explored CSM mass (i.e., $M_{\text{CSM}} = 0.05, 0.1, \text{ and } 0.15 M_{\odot}$) and CSM radius (i.e., $R_{\text{CSM}} = 10^{13}, 10^{14}, \text{ and } 10^{15}$ cm), and we find that

³¹ <https://sne.space/sne/>

Table 2
Explosion and Progenitor Properties

	Ic 2020oi	2007gr	1994i	Ic-BL 2020bvc	2020bvc	1998bw	2006aj
References ^a	this work	1, 2, 3	4, 5, 6	this work	Ho (7)	8, 9, 10, 11	12, 13, 14
C–O star (M_{\odot}) ^b	2.16	1	2.1	8.26		14	3.3
Explosion energy E_{exp} (10^{51} erg)	1			12			2.7
Kinetic energy E_K (10^{51} erg)	0.6	1–4	1	10.5	3	20	2
Ni mass (M_{\odot}) ^c	0.07	0.076	0.07	0.4	0.11	0.4	0.22
Ejecta mass (M_{\odot})	0.71	1.8	0.6	6.36	1.0	6.8	1.4
Progenitor (M_{\odot}) ^d	13	15	13–15	40–50		40	20
CSM mass (M_{\odot})	$\leq 3 \times 10^{-4}$			0.1	< 0.01		0.1
CSM R (cm)				10^{14}	$> 10^{12}$		3×10^{13}

Notes.

^a (1) Valenti et al. (2008); (2) Hunter et al. (2009); (3) Mazzali et al. (2010); (4) Iwamoto et al. (1994); (5) Sauer et al. (2006); (6) Immler et al. (2002); (7) Ho et al. (2020c); (8) Cano (2013); (9) Patat et al. (2001); (10) Li & Chevalier (1999); (11) Nakamura et al. (2001); (12) Mazzali et al. (2006); (13) Nakar & Piro (2014); (14) Waxman et al. (2007).

^b CO star mass is the progenitor mass at the pre-SN stage.

^c The ^{56}Ni distribution profile is a Gaussian function with $f_m = 5.0$ for SN 2020oi and a step function with $f_m = 0.9$ for SN 2020bvc (see Yoon et al. 2019, for details).

^d Progenitor mass here is the initial mass of the progenitor.

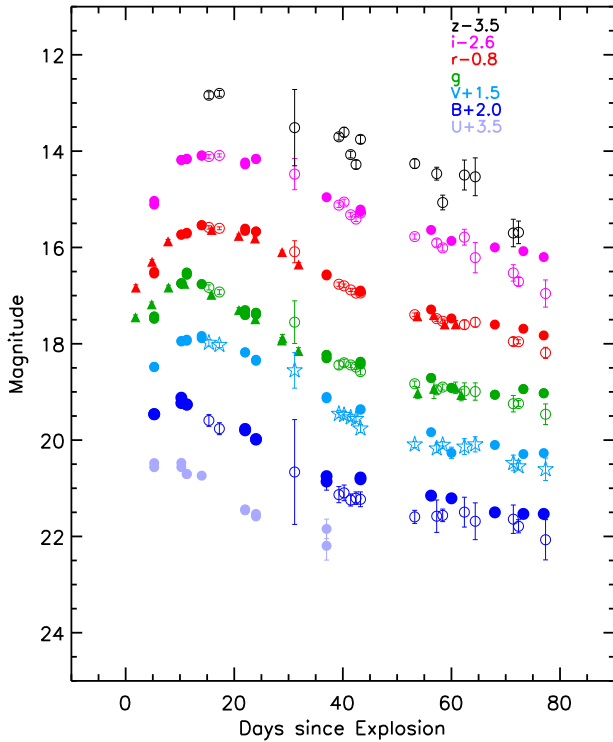


Figure 4. Multicolor light curves of SN 2020bvc from LCO (filled circles), Konkoly (open circles and stars), and ZTF (triangles) with days since the explosion. The explosion date of 2020 February 3 (MJD = 58,882) is between the last nondetection and the first detection from Ho et al. (2020c).

(The data used to create this figure are available.)

$M_{\text{CSM}} = 0.1 M_{\odot}$ and $R_{\text{CSM}} = 10^{14}$ cm ($\sim 1400 R_{\odot}$) give the best fit to the first peak of the light curves in the different bands. The estimated mass and radius of the extended material are comparable to those in other Type Ic (e.g., superluminous) SNe (Piro 2015). In Section 4.3, we compare the light curves of SN 2020bvc with other SNe Ic-BL and discuss possible scenarios to explain the double-peaked light curves.

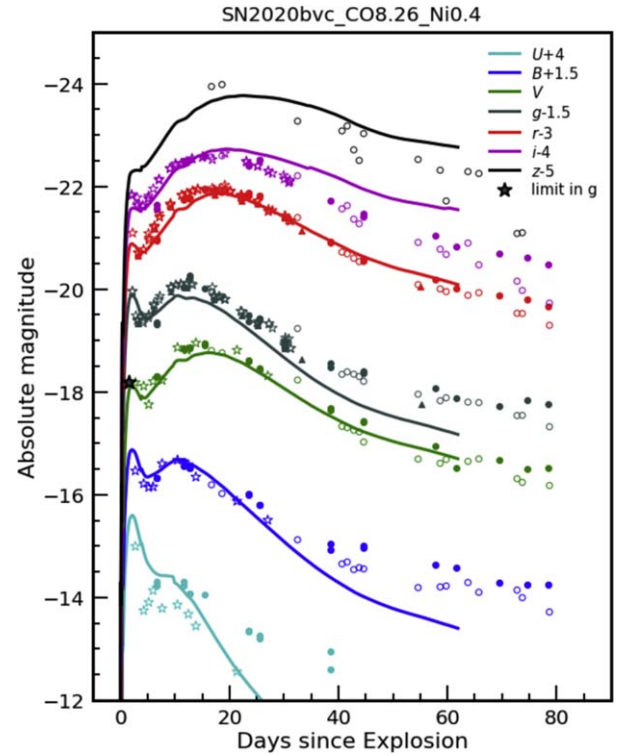


Figure 5. Light curves of SN 2020bvc (the double-peaked light curves from Ho et al. 2020c are denoted by star symbols) superposed on SN Ic model predictions from an $8.26 M_{\odot}$ CO star progenitor with explosion energy of 12×10^{51} erg, nickel mass of $0.40 M_{\odot}$, and CSM mass and radius of $M_{\text{CSM}} = 0.1 M_{\odot}$ and $R_{\text{CSM}} = 10^{14}$ cm. The inconsistency of U -band photometry between our LCO and SWIFT (Ho et al. 2020c) is due to the difference in filters.

3.4. Optical and NIR Spectroscopy of SNe Ic and SNe Ic-BL

Figure 6 shows 13 optical spectra of SN 2020oi and eight optical spectra of SN 2020bvc. Figure 7 shows four NIR spectra, along with the corresponding optical data from the nearest day of SN 2020oi and SN 2020bvc, together with the

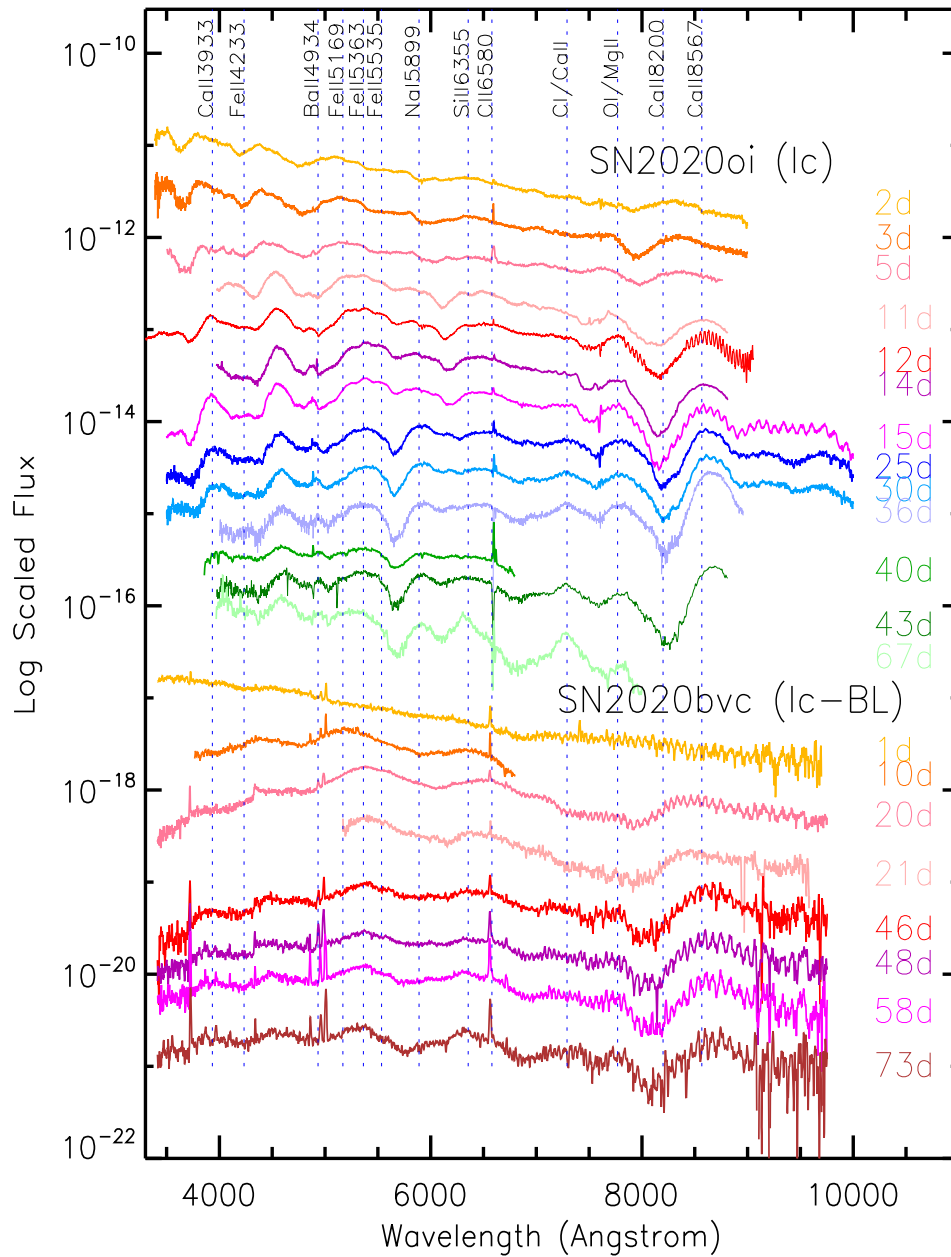


Figure 6. Optical spectra of SN 2020oi and SN 2020bvc with the LCO network, Bok, Lijiang, Xinglong, and SOAR telescopes (see Table 1 for details). At top, the wavelengths of noteworthy atomic lines (at rest wavelength) are indicated (where CaII8200 infers blueshifted Ca II triplets).

identifications of lines (see Table 1). The optical and NIR spectra of SN 2020oi span days 2–67, and those of SN 2020bvc span days 1–73. The rest wavelengths of the lines (note that we use angstroms in STP air for the optical spectra and microns in vacuum for the NIR spectra) are from the SN spectral models by Dessart et al. (2012) and synthesized spectra using SYNAPPS (Thomas et al. 2011), other observed spectra of SNe Ic (Hunter et al. 2009; Gerardy et al. 2002; Drout et al. 2016; Stevance et al. 2017, 2019), or SNe Ib (Ergon et al. 2014; Jencson et al. 2017).

The spectra of both SNe are dominated by atomic lines, in absorption or in emission, and sometimes simultaneously in the form of P Cygni profiles. In some cases, where multiple lines are thought to contribute, such as the NIR Ca II triplet, we refer to the combined lines as “features.” The species making the strongest contributions are Fe II, Si II, Ca II, C I, Si I, and Si I

(see Figure 7). The lines of Type Ic-BL SN 2020bvc are distinctly broader than those of Type Ic SN 2020oi. Surprisingly, despite their belonging to different subclasses of Type Ic, almost the same set of lines can be seen in each of them. The lines are labeled next to each peak: Fe II at 4924, 5018, 5169, and 5363 Å (Kankare et al. 2014), and Si II at 6355 Å. The Ca II IR triplet shows both absorption and emission (due to its members having P Cygni profiles). We use the mean wavelength of 8567 Å for the triplet, the wavelengths of whose individual lines are 8498, 8542, and 8662 Å. The absorption line at 1.01 μm is C I, and the nearby line at 1.046 μm is Si I with both absorption and emission in Figure 7. The lines of Si I at 1.113 μm, Fe II/Mg II at 1.47 μm, Si I at 1.589 μm, Fe II at 1.809 μm, and Fe II at 2.18 μm of SN 2020bvc also have counterparts in the spectra of SN 2020oi. The presence of these lines is consistent with the lines in SN 2011dh, SPIRITS 15 c

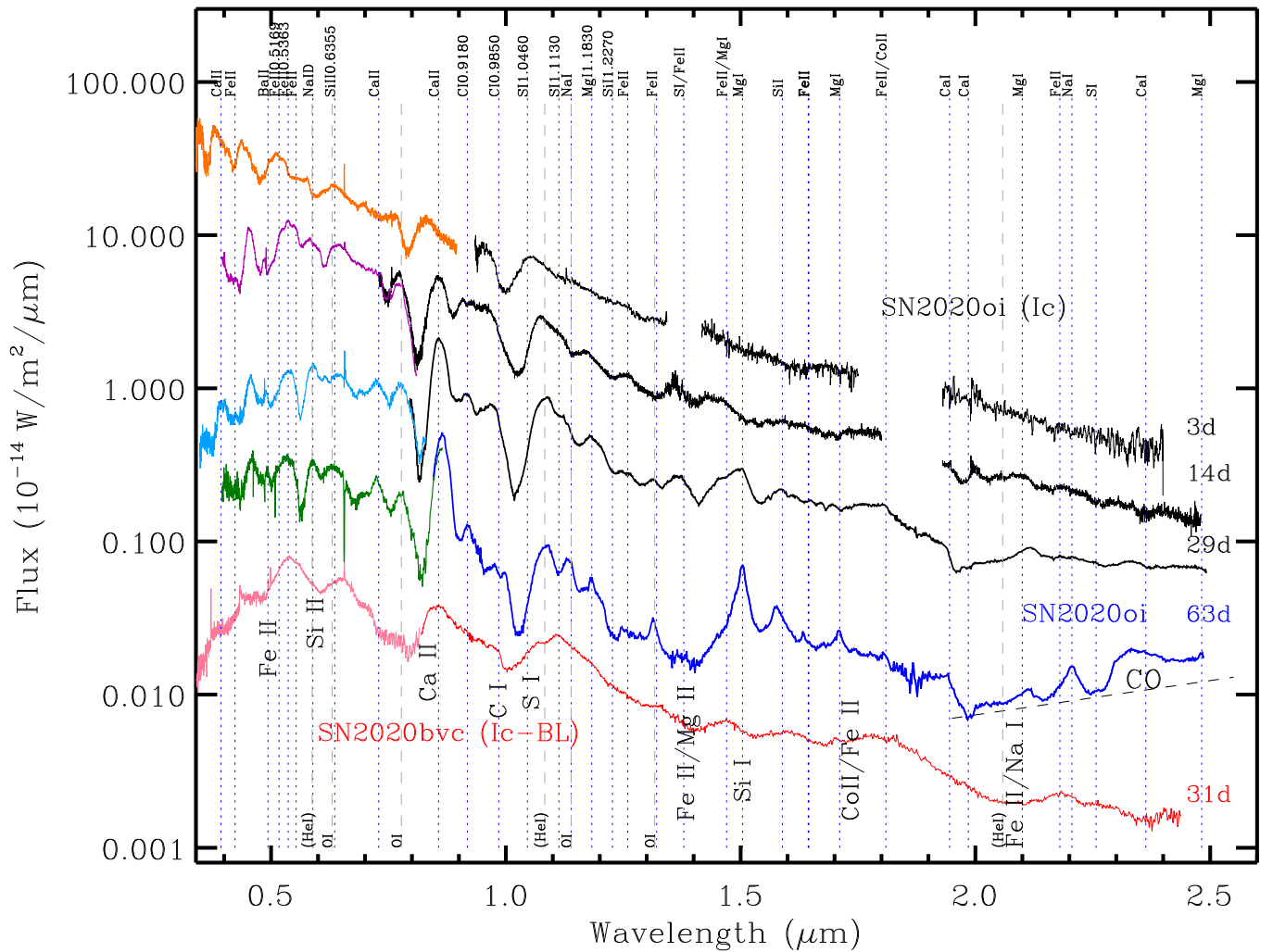


Figure 7. Optical and NIR spectra of SN 2020oi (top four) and SN 2020bvc (bottom in rose and red), shifted to $z = 0$. The optical spectra closest in time (see Figure 6 marked in the same color) to the dates of the infrared spectra have been adjoined to the infrared spectra. At the top the wavelengths of noteworthy atomic lines (at rest wavelength) are indicated, and at the bottom the broad lines observed in SN 2020bvc are identified. The dates (after explosion) at right are when the infrared spectra were obtained. The dashed line in the day 63 spectrum of SN 2020oi (in blue) is an approximate K -band continuum, and the location of the CO emission above it is indicated. The O I lines are marked in dashed-dotted lines with the labels at the bottom, blended with other lines. The locations of He I lines (at 0.5875, 1.0830, and 2.0581 μm) are marked with gray dashed lines and indicated at the bottom.

(Jencson et al. 2017), and SN 2007gr (Hunter et al. 2009). The Fe II at 1.64 μm and Mg I lines at 1.5 μm are commonly detected in SN Ib/Iib SPIRITS 15 c (Jencson et al. 2017), as well as in SN IIP SN 2017eaw (Rho et al. 2018a). There is little temporal change in the spectra of SN 2020bvc from 20 to 73 days. The spectrum at 1 day is mostly blackbody emission, and the peak emission wavelength in the spectrum at 10 days is different from those at 20–73 days. The velocity profiles of the line features are discussed in Section 4.2.

Lines of He are present at 5875 \AA , 1.083 μm , and 2.0587 μm . At 5875 \AA , there is also an Na I line (Figure 6), and at 1.083 μm , the Si I line is present (Figures 7). The He I line at 2.0587 μm is free of other lines. However, at high velocity, the absorption of this line in SN 2020oi is potentially present. The presence and velocity profiles of He lines are discussed in Sections 4.2.1 and 4.4.

The spectral signature of the CO overtone band emission at 2.3–2.5 μm with its “sharp cut-on” on the short-wavelength edge is clearly evident in the day 63 spectrum of SN 2020oi; it was not present at day 29. Band heads of CO occur at 2.294, 2.323, 2.353, 2.383, 2.414, 2.446, and 2.447 μm (see Figure 2

of Rho et al. 2018a). Only the cut-on due to the shortest-wavelength band head is apparent. This is due to a combination of the high-velocity width and the optically thick CO gas that makes up the individual bands.

Longward of 2.0 μm , the continuum flux density from SN 2020oi increases on day 63, whereas it was decreasing in the earlier spectrum. This is an unambiguous detection of warm dust. Detection of dust in Type Ic spectra is rare, especially at such early times.

4. Discussion

4.1. CO and Dust Formation in Type Ic SN 2020oi

4.1.1. CO Properties from LTE Model

CO is one of the most powerful coolants in the ejecta of SNe II and is believed to be responsible in large part for cooling the ejecta to temperatures at which dust can form. It is questionable as to whether the models accurately represent the evolution of the ejecta and their mixing. Still, it is clear that measurements of CO are important tests of them, and the presence of CO is

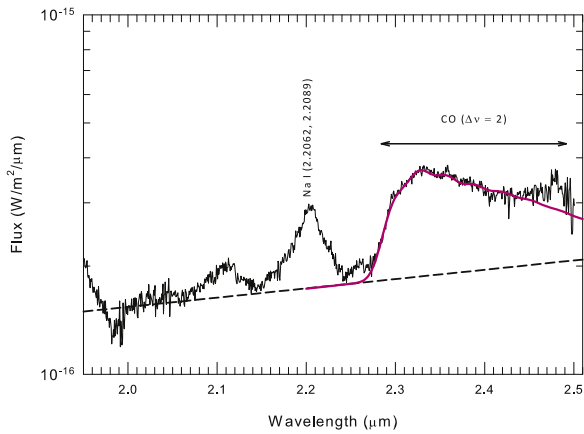


Figure 8. Emission from the CO first-overtone bands in SN 2020oi on day 63 shown in black, on which is superposed the best LTE model fit (red line), which has the following parameters: temperature of the CO gas = 3150 K, velocity = 3700 km s⁻¹, and mass = $0.8 \times 10^{-4} M_{\odot}$. The adopted continuum is shown by the dashed line. More details are provided in the text.

closely tied to dust formation. The onset of CO formation in SNe is best seen in the first-overtone bands at 2.3–2.5 μm , which have been detected only in a handful of CCSNe (e.g., Sarangi et al. 2018).

We have estimated the CO mass in SN 2020oi using the LTE model developed by Das et al. (2009), which assumes optically thin emission and a pure $^{12}\text{C}^{16}\text{O}$ composition. Earlier applications of the model include SN 2017eaw (Rho et al. 2018a), SN 2016adj (Banerjee et al. 2018), and several novae (Banerjee et al. 2016; Joshi et al. 2017). We adopted a straight continuum (for the dust emission) passing through the two minima (2.01–2.08 μm and 2.155–2.17 μm) in the spectrum between 2.00 and 2.23 μm . The best-fit model, shown in Figure 8, was determined by varying the CO mass, temperature, and velocity dispersion using chi-square minimization over the region 2.27–2.44 μm . The region beyond 2.44 μm was excluded from the fit optimization owing to spectral contamination caused by a strong atomic line at $\sim 2.48 \mu\text{m}$, possibly due to Mg I. We estimate the following parameters for the CO gas: temperature = 3150 ± 200 K, velocity = 3700 ± 100 km s⁻¹, CO mass = $(0.7\text{--}0.9) \times 10^{-4} (d/16.22)^2 M_{\odot}$, where d is the actual distance in Mpc.

The estimated CO mass of SN 2020oi is the first estimate for an SN Ic. The CO mass of $\sim 10^{-4} M_{\odot}$ is consistent with those observed in other SNe (e.g., SN 1987A; Sarangi et al. 2018, and references therein) at similar epochs. Models of CO formation for SNe IIP (e.g., Sarangi & Cherchneff 2013; Sluder et al. 2018) indicate that the amount of CO increases from $\lesssim 10^{-4} M_{\odot}$ at 100 days since the explosion to as much as $0.1 M_{\odot}$ after $\gtrsim 1500$ days, irrespective of SN progenitor (see, e.g., Sarangi & Cherchneff 2013). CO was detected in SN Ib SN 2016adj at day 58 after discovery, and its estimated CO mass was $2 \times 10^{-4} M_{\odot}$ (Banerjee et al. 2018).

The detection of CO in SN 2020oi, only ~ 63 days since the explosion (~ 54 and 52 days after B - and V -band maximum, respectively), is one of the earliest CO detections in an SN of any type. There are only two other SNe where a similar, early CO detection was made, namely, SN 2013ge (Drout et al. 2016) and SN 2016adj (Banerjee et al. 2018). Detections of CO were reported in SN Ic SN 2000ew and SN 2007gr at day 90 and 70 (post- B maximum), respectively (Gerardy et al. 2002; Hunter et al. 2009). Sarangi et al. (2018), summarizing data

obtained up to 2013, found only four CO detections before day 100. In this context, the early onset of CO formation in SNe, such as SN 2020oi, may present a serious challenge for theoretical models.

4.1.2. Non-LTE CO Model: Diatomic Molecule Formation as a Diagnostic

As a second approach to molecular formation, we consider spherical explosion models with the free parameters as follows: (1) the progenitor mass, (2) the initial stellar density and abundance structure, (3) the explosion energy and amount of ^{56}Ni , and (4) possible mixing processes as key to the inherently 3D nature of the CCSN explosion mechanism. Parameters 1–3, which characterize the explosion model, can be derived from light curves and spectra.

We demonstrate in the Appendix that the structure of the molecular bands of CO and CO⁺ provides a sensitive tool to probe the temperature, velocity, and chemical composition and that a large CO⁺/CO indicates the exposure to hard radiation in the CO-emitting region, which depends on mixing.

As described below, further information on mixing comes from the time dependence of the strength of the CO feature. In CCSNe with massive H-rich envelopes, the onset of the CO formation is correlated with the photosphere entering the CO core as discussed below. However, in SNe Ic, the CO core is exposed from the beginning, and the photosphere is hot. Thus, ^{56}Ni mixing may play the central role in the onset of CO formation rather than low T .

Mixing in Light of the Explosion Physics.—Large- and small-scale mixing is not well understood, but polarization measurements of another Type Ic, SN 2002ap, and the Type IIB SN 2001ig suggest a large-scale bipolar abundance structure (Wang et al. 2003; Maund et al. 2007), which is consistent with asymmetric, axially symmetric explosion mechanisms (e.g., Hoeflich et al. 1999; Khokhlov et al. 1999; Couch 2017). Spherical explosions form a central cavity and a dense shell supported by radiation pressure. In contrast, a large-scale asymmetric explosion does not form a central cavity because material is dragged down, and the void is filled. As shown in the papers cited above, the detailed structure depends on various mechanisms that include Rayleigh–Taylor instabilities of the shell, asymmetric explosions by bipolar outflows, angular momentum inherited from the progenitor, etc., which result in different density and abundance profiles. Here we assume that mixed material fills the inner void and use mixing of abundances of the parts of the core as a free parameter and the molecule formation as an indicator.³²

Model Setup and Methods.—We consider the questions whether and under which condition molecular formation can be understood in SNe Ic such as SN 2020oi.

We simulate the time-dependent molecule formation via rate equations and radiation transport as affected by the optical depth of the CO lines. We use the dynamical background based on the progenitor and the explosion parameters for SN 2020oi found by the light-curve analysis of Yoon (2017) and Yoon et al. (2019) with mixing of the ejecta as a free parameter. For our simulations, we use our HYDrodynamical RADIATION code

³² In the spherical explosion model for SN 2020oi, the inner cavity has a size of ≈ 6000 km s⁻¹, which is inconsistent with the velocity indicated by the CO feature. As we will see below, the resulting low density due to large geometrical dilution causes CO formation timescales that are inconsistent with the early CO observed in SN 2020oi.

HYDRA, which includes modules to provide a solution for the nuclear networks, the statistical equations needed to determine the atomic level population, the equations of state, the opacities, the hydro in comoving hydro via the piecewise parabolic method, and radiation/positron transport problems (Hubeny & Lanz 2003; Kubát 2009; Hoefflich et al. 2019). These modules have been widely applied in non-LTE analyses of SN 1987A and of SNe of Type II, Ibc, and Ia.

For the background and computational efficiency, we use the same assumptions as for SN 1994I (Hoefflich et al. 2000), an approach very similar to STELLA. The photon transport in molecules is solved in the comoving frame without relativistic corrections (Mihalas et al. 1975; Mihalas & Mihalas 1984) and formal integration for the emitted spectrum because the CO emission is not optically thin and can be expected to have an effect on estimates of the amount of CO required. Our Monte Carlo scheme is used for γ -transport (Hoefflich et al. 1993; Penney & Hoefflich 2014) because the ionization may affect the timescale of the CO and CO⁺ formation as has been widely discussed for SN 1987A (Hoefflich et al. 1989; Spyromilio et al. 1989; Lepp et al. 1990; Meikle et al. 1993). We use our module for molecule formation. For details, see Sharp & Hoefflich (1990, 1989), Gerardy et al. (2000), and references therein. For the formation and destruction, we use the time-dependent rate equations for $C + O \rightarrow CO$, $C^+ + O \rightarrow CO^+$. For the simulations below, typical 50,000 to 300,000 rovibrational transitions have been taken into account for each CO, CO⁺, and SiO. SiO are included because the progenitor model has overlapping chemical regions with C, O, and Si. Depending on the conditions, Si can bind O, which then is not available for CO formation. As is common for the time-dependent networks (e.g., Meikle et al. 1993), we include three-body association with neutral and singly ionized C and O, radiative association and dissociation, collisional dissociation by electrons, and charge-exchange reactions. In addition, the energy deposition and ionization by radioactive decay, γ -rays, and positrons are taken as additional ionization processes for both the atoms and molecules. Note that for SN 1987A, the importance of the CO⁺ channel is still under debate (Petuchowski et al. 1989; Sharp & Hoefflich 1990). However, γ -ray escape was small in SN 1987A at the time of the CO formation, whereas in an SN Ic we see directly the exposed core strongly formed by asymmetric explosions and conditions in which nonthermal excitation and ionization occur.

4.1.3. Application of Non-LTE CO Model to the NIR Spectrum of SN 2020oi

The discussion above revealed signatures but leaves unanswered questions on the time dependence of CO and regarding optical depth effects at some 48 days past maximum or 2 months after the explosion. Can we understand the early CO formation needed in SN 2020oi, and what amount of CO is needed?

Note that each model requires a time series of γ -ray and positron transport, as well as radiation transport simulations for some 1000 time steps. Therefore, we assumed full mixing up to a certain velocity only. For the case of unmixed models, the hydrodynamical profile is used, which contains a density “hole” as in the model. For mixed models, we assume that the density hole is filled (Figure 9). Nonthermal processes will enter by positrons and γ -rays. In all of our models, the positron component is local, while the γ -ray deposition is mostly nonlocal. Thus, the effect on molecule formation will depend

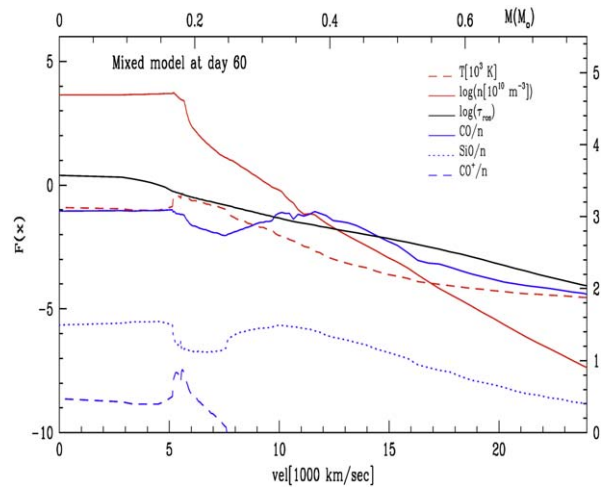


Figure 9. Structure of the mixed model at day 60. We give temperature T and particle density n (right scale) and the τ_{ros} particle abundances of CO, CO⁺, and SiO as functions of $F(x)$ of the expansion velocity (lower scale) and mass (top scale). The expansion velocity of 5000–9000 km s⁻¹ of SN 2020oi (see Section 4.2) infers a temperature of 3000–3300 K and a density of $(3\text{--}5) \times 10^4 \text{ cm}^{-3}$.

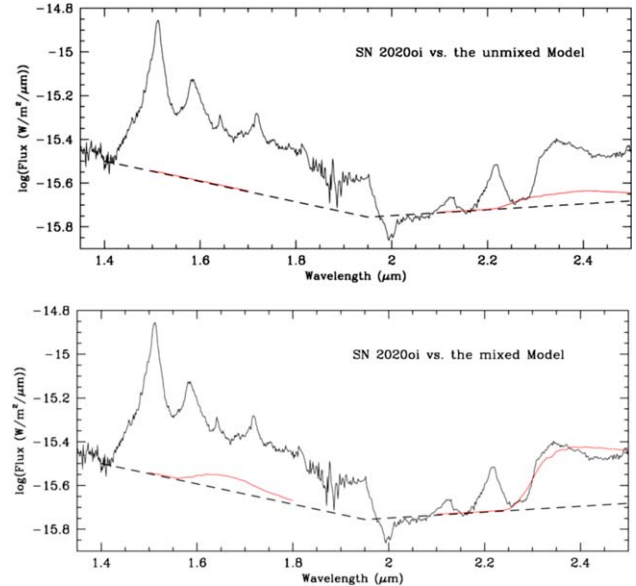


Figure 10. Comparison between the CO contribution to the flux by time-dependent non-LTE models (red) and SN 2020oi (black) in the spectral regions of the first and second overtones of the CO bands (at 2.3–2.5 μm and 1.6–1.8 μm , respectively). Dashed lines are estimated continua. To produce a CO core early on, large-scale mixing of the core is needed. See text for details.

somewhat on homogeneous or large-scale mixing, but we found this effect on the CO emission spectrum to be small.

As an error estimate for the mass of the CO we only quote the variation possible within these simple assumptions. Obviously, the formation depends on model parameters not considered, such as clumps in both chemistry and density, large-scale asymmetry, etc. Instead, we calculated a series of models with various amounts of core and ⁵⁶Ni mixing to fit the observations.

In Figures 9 and 10 we show the structure of the mixed model (up to $v \approx 7000 \text{ km s}^{-1}$) and the comparison between the observed and theoretical spectra of the mixed and unmixed model. Both models show some CO beginning about 50 days after the explosion. This phase coincides with the transition

from the optically thick regime τ_{ROS} to the optically thin regime, as it allows for effective cooling of the deeper, dense layers as a prerequisite for molecule formation.

The early formation of CO is directly linked to low ejecta mass. CO formation would set in later for more massive envelopes because of the more effective trapping of thermal energy. Charged reactions are important for CO formation. In the inner hotter layers, a large fraction of the CO production occurs at the “photosphere” via the CO^+ channel, as the photosphere recedes with time. However, even in our models, the rate $d\text{CO}^+/dt$ is larger than the expansion time, leading to the overall low CO^+ concentration seen in Figure 9. Note that without extensive mixing, the CO formation timescales are much longer or the formation is even suppressed and the CO forms well above the photosphere. As a result, the CO feature in our unmixed model is both too weak and too broad (Figure 10).

In the following we discuss the mixed model using the first overtone of CO. About 0.5%–1% of the total carbon is bound in molecules. CO is important for the coupling between the radiation field and the plasma. However, only a small amount, $\approx 10^{-3} M_{\odot}$, is in the optically thin regime and contributes to the emission. The lower vibrational modes of the first CO overtone only become optically thin at $\approx 6000\text{--}8000 \text{ km s}^{-1}$. This leads to rather featureless synthetic CO-spectral profiles as observed. However, the overly broad blue wing to the first band head ($2.3 \mu\text{m}$) and the suppression of the flux at the peak may indicate an excess of CO formation at the time prior to the observation.

The second CO overtone (at $\sim 1.6\text{--}1.8 \mu\text{m}$) is weak and does not conflict with the observations, which did not detect it. It may contribute to the flux at the $\approx 10\%$ level, but atomic lines of allowed transitions still dominate the spectrum at day 60 until much later, namely, the nebular phase. With mixing there is significant formation of SiO even some 2 months after the explosion that might be detected. As discussed in Section 4.1.2, layers with excess Si versus C should show a strong feature if the Si core is exposed or Si/O compositions are mixed on a macroscopic scale. With time, deeper layers become sufficiently cool for SiO to form. Combining NIR CO and mid-IR (MIR) SiO would provide a unique tool to distinguish various models and physical mechanisms. Temperatures are too high for early dust formation, which, in SN 2020oi, may favor the interpretation of preexisting dust likely being heated by the SN radiation over the formation of new dust.

For SN 2020oi low ejecta mass, extended mixing and explosion mechanisms that can “fill the inner void” are needed to match the observations. SN 2020oi is an important representative of the “low”-mass end of SNe Ic, with SN 1994I being the only other representative. Our analysis of the CO feature shows that mixing of the inner region is needed from both its strength and profile. The spectral feature probes both the velocity and the time domain. The light curves only make use of the time domain and, thus, are less suitable to probe mixing and asymmetries. At early times, mixing and asymmetries will mostly change the shape of the light curves. To first order, the rise is dominated by the mass and energy of the ejecta, whereas late times are dominated by the amount of ^{56}Ni . The angular redistribution of photons is largest at early times. At late times, the radiation becomes isotropic. A full 3D light-curve analysis is beyond the scope of this paper.

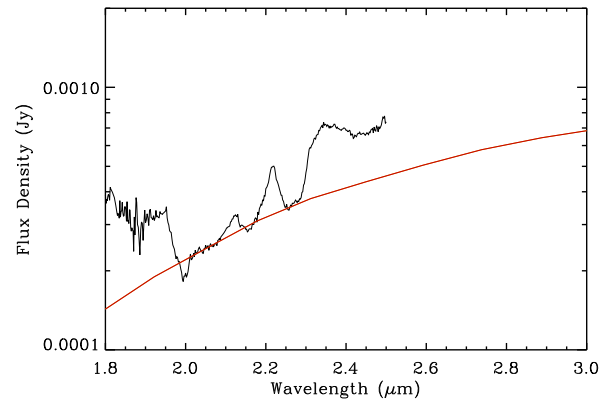


Figure 11. Spectrum of SN 2020oi at 63 days superposed on a carbon dust model (in red) for the best-fitting dust temperature of $\sim 810 \text{ K}$. We performed the fitting only using the continuum between 2.00 and $2.32 \mu\text{m}$. The best-fit model is plotted from 1.8 to $3 \mu\text{m}$ for display purposes.

4.1.4. Dust Emission in SN 2020oi

As can be seen in Figure 7 at day 63, the spectrum of SN 2020oi exhibits a rising continuum flux density longward of $2.0 \mu\text{m}$, as well as emission from CO longward of $2.3 \mu\text{m}$. Clearly, the rising continuum is due to emission from dust. The dust continuum is fit with the Planck function ($B_{\nu}(T)$) multiplied by the absorption efficiency (Q_{abs}), where we assume carbon dust and the best fit is shown in Figure 11. We use carbon dust because it condenses early, at temperatures $1100\text{--}1700 \text{ K}$ (Fedkin et al. 2010). The continuum we use is similar to that for the CO analysis (in Sections 4.1–4.3), but we add the third portion between 2.255 and $2.285 \mu\text{m}$ in addition to the two parts between 2.01 and $2.08 \mu\text{m}$ and between 2.155 and $2.17 \mu\text{m}$ since Q_{abs} of carbon dust has a curvature. Details of the fitting procedure using MPFIT (Markwardt 2009) and information about absorption coefficients are given in Rho et al. (2018b). The estimated dust temperature is $810 \pm 10 \text{ K}$, and the dust mass is $(5.9 \pm 0.7) \times 10^{-5} M_{\odot}$. There may be another lower-temperature dust component, but we cannot constrain it since the CO feature (see Figures 8 and 10) continues at the end of the spectrum (at $2.5 \mu\text{m}$). Spectral coverage beyond $2.5 \mu\text{m}$ is required to estimate a more accurate dust mass. Therefore, the dust mass of $(5.9 \pm 0.7) \times 10^{-5} M_{\odot}$ is a lower limit of the dust mass.

Two key questions about the emitting dust need to be addressed: (1) Is the rising continuum emitted by freshly formed dust in the SNe ejecta? (2) Can dust form as early as at 63 days post-explosion in SNe Ic? Dust formation in SNe Ib has been observed in the case of SN 2006jc. SN 2006jc showed increasing NIR flux excess as early as 50–75 days based on photometry (Di Carlo et al. 2008) and a rising continuum in optical spectra, indicating a dust temperature of 1700 K and dust mass of $6 \times 10^{-6} M_{\odot}$ (Smith et al. 2008). The dust emission at day 50 seen in SN 2006jc was interpreted as being due to either new dust in the ejecta or dust originating from the dense shell formed in the post-shock CSM (Smith et al. 2008; Pastorello et al. 2008). On day 20, AKARI observation of SN 2006jc detected NIR to MIR emission that can be fitted with a two-temperature dust model with 800 and 320 K and corresponding dust masses of $7 \times 10^{-5} M_{\odot}$ and $2.7 \times 10^{-3} M_{\odot}$, respectively (Sakon et al. 2009). The 800 K dust component is suggested to originate from freshly formed dust, and the 320 K component is in the CSM dust.

Freshly Formed Dust: The central region of CO in SN 2020oi is optically thick so that radiation from CO does not efficiently cool the gas to low-enough temperatures for the dust to form. The temperature in the CO-forming region is ~ 3000 K. In the outer layers (see Figures 9 and 10), where CO can cool the gas efficiently, densities are too low ($\sim 4 \times 10^4 \text{ cm}^{-3}$) by many orders of magnitude for dust formation. Note that this conclusion assumes a progenitor and fully mixed model as described earlier. Our dust-forming model based on Dominik (1992) and Dominik & Tielens (1997), which is an extension of the non-LTE CO modeling (Sections 4.1.2 and 4.1.3), shows that no prominent dust forms at day 63 in the Type Ic SN 2020oi. However, chemically controlled dust models tend to result in earlier dust formation (Sarangi & Cherchneff 2015; Sluder et al. 2018), and clumping of ejecta may change the timescale of dust formation.

The presence of newly formed dust in either ejecta or CSM interaction can be tested by other means. One possible signature of dust formation is a deviation in the light curves from those produced purely by the ^{56}Co -to- ^{56}Fe decay slope (Elmhamdi et al. 2004). An example is SN 2006jc, which shows such a deviation around day 60, as shown in Figure 3. SN 2020oi does not show a significant deviation from the decay slope between days 20 and 60. Another signature of newly formed dust can come from line profiles. The red wings of emission lines can be suppressed owing to extinction by newly condensing dust that obscures the receding gas. Dominant blue wings relative to red wings, or double-peaked line profiles due to condensing dust, are often observed in hydrogen or helium lines (Elmhamdi et al. 2004; Smith et al. 2008), but SN 2020oi did not display such line profiles. Bevan et al. (2019) have attributed the early-time (~ 70 -day) line profile asymmetries in SN 2005ip (Type IIn) to newly formed ejecta dust rather than a CSM shell, although the dust mass at day 50 is only $10^{-8} M_{\odot}$. Atomic lines in the optical or NIR spectra at day 63, which contains CO emission and a rising dust continuum (Figure 7), do not show any asymmetry or other unusual line shapes. Note, however, that spectra obtained after day 63 are too limited to reveal any temporal change, because the spectra lack hydrogen and helium lines.

A model of Type Ib SN 2006jc by Nozawa et al. (2008) indicates that carbon dust formation can occur in SNe Ib as early as at 40–60 days owing to the rapid decrease in the gas temperature in SNe Ib. This is consistent with the carbon dust we used in our dust fitting of SN 2020oi above. The temperature at day 50 reaches 1000–2000 K, and carbon dust forms in the outer carbon layer. The condensation of carbon dust is followed by the condensation of silicate and oxide grains, up to 230 days; most of the dust forms at days 80–180 (Nozawa et al. 2008). Compared to SNe IIP, SNe Ib/Ic have lost most of the hydrogen/helium envelopes before the explosion; thus, their ejected masses are smaller, and the expansion velocities are higher than in SNe IIP. This leads to a lower density of gas in the ejecta and more rapid cooling than in typical SNe II. The dust temperature and dust mass that we derive for SN 2020oi are comparable to those in the dust formation model for SN 2006jc of Nozawa et al. (2008).

The equilibrium temperature of the dust T_d is determined in the usual way by assuming radiative balance between absorption and emission:

$$\frac{L_*}{4\pi r^2} \bar{Q}_{\text{abs}} \pi a^2 = 4\pi a^2 \sigma T_d^4 \langle Q_{\text{abs}}(T_d) \rangle,$$

where L_* is the bolometric luminosity of the central object, r is the distance from the SN that the dust has reached at time t , and σ is the Stefan–Boltzmann constant. \bar{Q}_{abs} is the absorption efficiency of the dust, averaged over the SED of the heating source, and $\langle Q_{\text{abs}}(T_d) \rangle$ is the Planck mean absorption efficiency of the dust. For carbon dust we take $\bar{Q}_{\text{abs}} \simeq 1$ and $\langle Q_{\text{abs}}(T_d) \rangle = 1.0 \times 10^{-4} a T_d$, where a is the grain radius in μm ; this formulation for $\langle Q_{\text{abs}}(T_d) \rangle$ is valid for $250 < T_d(\text{in K}) < 1000$ and $a < 0.3 \mu\text{m}$ (see Tielens 2005, for details). Thus,

$$T_d = \left(\frac{L_*}{16\pi r^2} \frac{1}{10^{-4} a \sigma} \right)^{1/5}$$

$$T_d(\text{in K}) \simeq 16.8 \left(\frac{L_*}{L_{\odot}} \right)^{1/5} \left(\frac{r}{10^{17} \text{ cm}} \right)^{-2/5} \left(\frac{a}{1 \mu\text{m}} \right)^{-1/5}.$$

We derive the luminosity of SN 2020oi at day 63 using optical photometry to be $2.5 \times 10^{40} \text{ erg s}^{-1}$, but this does not include the ultraviolet contribution. The luminosity from our light-curve model gives $L_* = 1.5 \times 10^{41} \text{ erg s}^{-1}$ for the bolometric luminosity, which is consistent with the smallest luminosity of SNe Ic (Kumar et al. 2018); we use this value for L_* in what follows.

As the ejecta are strongly decelerating (see Figure 12), we estimate the distance reached at time $t = 63$ days by assuming for simplicity that the ejecta velocity declines with time as $v_{\text{ejecta}} \propto t^{-\alpha}$, where α is a small positive constant. This is intended for convenience only and clearly not as a physical model. We integrate v_{ejecta} over time, using the times and velocity values for the Ca II $\lambda 8567$ line and the [S I] 1.046 μm line in the caption of Figure 12. We find that $\alpha \simeq 0.22$ for the Ca II line and $\alpha \simeq 0.29$ for the [S I] line. In this way we find that $r \simeq 2.6 \times 10^{17} \text{ cm}$ from the Ca II line and $r \simeq 9.3 \times 10^{16} \text{ cm}$ from the [S I] line. These values of r lead to $T_d \simeq 625$ (395) K and 945 (595) K, respectively, for a grain size of 0.1 (1) μm . Based on SN dust formation models (Sluder et al. 2018; Sarangi & Cherchneff 2015), the peak of grain sizes is close to 0.1 μm , although $\sim 1 \mu\text{m}$ size grains still exist. These values are in line with the value deduced ($T_d \sim 800$ K) from the IR excess.

These considerations point to the fact that the dust contributing to the IR excess of SN 2020oi in Figure 11 arises from dust condensing in the SN ejecta.

CSM Dust: Other possibilities to explain the rising continuum seen in SN 2020oi are that the emission originates in the preexisting CSM by the radiative heating of preexisting CSM dust by SNe or by newly formed dust in the swept-up CSM dense knots. The newly formed dust can result from the CSM interaction when the reverse shock hits the dense CSM shell or knots. In the case of SN IIn SN 2005ip, Fox et al. (2010) suggested that the warmer dust with temperature 900–1100 K and mass $\sim 5 \times 10^{-4} M_{\odot}$ originates from newly formed dust in the ejecta, or possibly the cool, dense shell, and is continuously heated by the interaction of the ejecta with the preexisting CSM. A cooler dust component with a temperature of ~ 300 K was also observed in SN 2005ip, which they suggested originated from heated dust.

For the Type IIn SN 2010jl, Andrews et al. (2011) estimated the temperature of its preexisting CSM dust shell to be ~ 750 K on day 90, which is comparable to the dust temperature we estimate for SN 2020oi on day 63. Gall et al. (2014) suggested

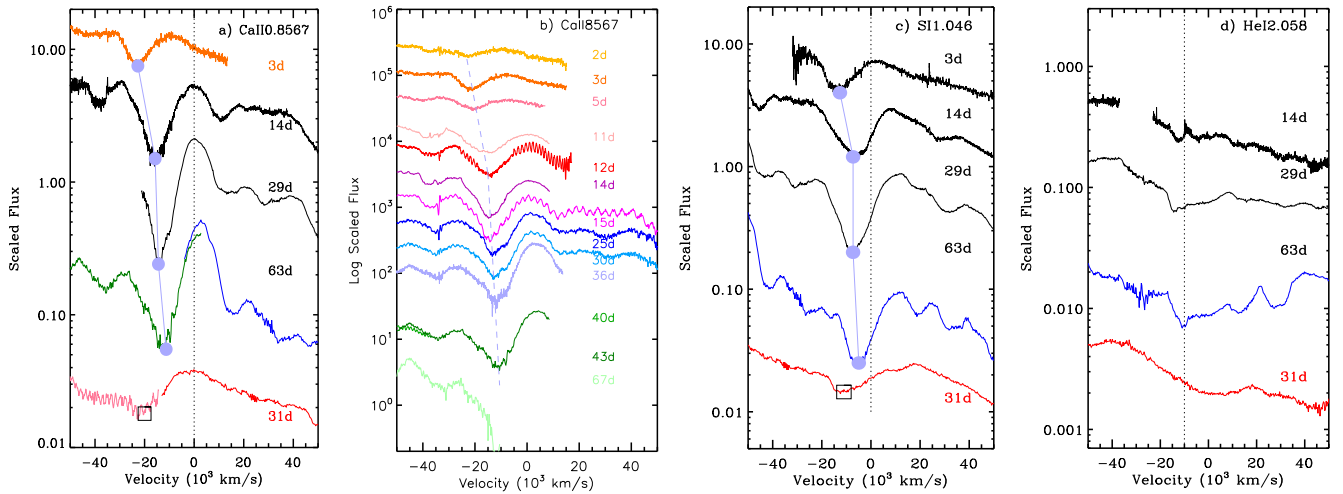


Figure 12. (a) Velocity profiles and temporal evolution of (a) the Ca II triplet (assumed intensity-weighted rest wavelength $0.8567 \mu\text{m}$) in SN 2020oi (upper four curves) and in SN 2020bvc (bottom curve in red). Color-coding is as in Figure 7 for NIR spectra (panels (a), (c), (d)) and as in Figure 6 for optical spectra (panel (b)). The Ca II triplet in SN 2020oi has both emission and absorption components; the velocities of absorption minima (in cyan) are marked in circles at the velocities $-22,700$, $-15,700$, $-14,400$, and $-11,300 \text{ km s}^{-1}$ for days 3, 14, 29, and 63, respectively. The velocities are estimated using Gaussian fits. (b) Same as panel (a), but for the Ca II optical line in SN 2020oi. Note the change in slope of the peak absorption velocity with time in both Ca II lines after the maximum peak at day 12. (c) Same as panel (a), but for the IR Si I line at $1.046 \mu\text{m}$ in both SNe. The absorption minima are at velocities of $-12,700$, $-7,300$, $-7,300$, and $-5,000 \text{ km s}^{-1}$ for days 3, 14, 29, and 63, respectively. (d) Same as panel (a), but for the potential He I line at $2.0587 \mu\text{m}$ in both SNe. The absorption minima are about $-10,000 \text{ km s}^{-1}$ (dotted line). The He I absorption feature is discussed in Section 4.4.

that the formation of dust between days 40 and 240 occurs in the dense CSM of SN 2010jl. However, the theoretical model by Sarangi et al. (2018), which included the heating of the post-shock gas, indicated that dust formation could only commence after day ~ 380 after the radiation from the shock weakens for the case of an SN II_n. We conclude that the observed dust in SN 2020oi may be preexisting, radiatively heated dust from a circumstellar shell.

IR Echo: An alternative interpretation of the dust emission is that it is due to an infrared echo (see Bode & Evans 1980a, 1980b). The SN outburst heats the preexisting dust (the dust shell of the progenitor or interstellar dust in the vicinity of the SN), which emits IR in moving features. *Spitzer* detected an IR echo in SN 2004et with a temperature of $115 \pm 15 \text{ K}$ from the ISM dust of the host galaxy (Kotak et al. 2009). The dust knots producing the echo in the young SNR Cas A show a similar temperature, $\sim 150 \text{ K}$ (Dwek & Arendt 2008).

Graham & Meikle (1986) show how to discriminate between dust condensation and an IR echo: from the color temperature of the dust to determining the distance, and hence the speed of recession, of the dust from the SN. Light-travel-time effects result in the bulk of the observed IR dust emission arising at the vertex of a paraboloid of revolution with focus at the SN, from which the vertex recedes at speed $c/2$, with c being the light speed (Graham & Meikle 1986; Dwek & Arendt 2008). The grain temperature at the vertex may in principle have any value up to the grain vaporization temperature (e.g., Graham & Meikle 1986), as the initial dust temperature observed for SN 1982e is $\sim 1300 \text{ K}$. The dust temperature of the IR echo depends on the SN burst luminosity and properties of preexisting dust that produce diverse SEDs (Dwek & Arendt 2008). The dust temperature of 810 K observed in SN 2020oi is therefore not inconsistent with an infrared echo.

In summary, the fact that the observed dust temperature is consistent with the equilibrium dust temperature from the SN raises the possibility that the rising continuum can come from newly formed dust either in the ejecta or in circumstellar knots.

However, heated dust from a circumstellar shell or an IR echo is still a plausible explanation for the rising continuum. Distinguishing between dust freshly formed in the SN ejecta, an IR echo, and dust formed in a preexisting CSM shell requires a higher sampling of dust emission with time. For heated dust, one would observe that the dust temperature increases with time. More frequent sampling of IR spectra between days ~ 20 and ~ 63 may be able to determine the changes in the dust temperature unambiguously. This, combined with a pathway and diagnostics of CO and SiO features from NIR/MIR observations as described in the Appendix, are crucial for advancing understanding of molecule formation/destruction and dust evolution in CCSNe, which will be investigated in greater detail and to later (fainter) stages of evolution during the era of JWST.

4.2. Spectral Evolution of Type Ic and Ic-BL

4.2.1. Velocity Profiles of Type Ic SN 2020oi

Many spectral lines, including multiple atomic line features of Fe II and Si II, appeared in the optical band (Figure 6). It is often difficult to determine whether the spectra features are due to different atomic lines or due to temporal velocity changes of the same line. Therefore, we use the strong absorption feature produced by the IR Ca II triplet at $0.8567 \mu\text{m}$, which appears in both the optical and NIR spectra (see Figures 6 and 7) as a guide. Figures 12(a) and (b) show the velocity profiles and temporal evolution of the Ca II triplet. We also show the velocity profiles of Si I at $1.046 \mu\text{m}$ and temporal changes in Figure 12(c).

We estimated velocities at the absorption dip (at minimum intensity) by fitting multiple-Gaussian components as needed; the components include both absorption and emission features. The velocity of the Ca II (Si I) peak absorption changes from $-22,700$ to $-15,700 \text{ km s}^{-1}$ ($-12,700$ to -7300 km s^{-1}), a change of 7000 (5400) km s^{-1} between the explosion and day 14, but between day 14 and day 63 the velocity changes only by 4400 (2300) km s^{-1} using NIR spectra complimented by the

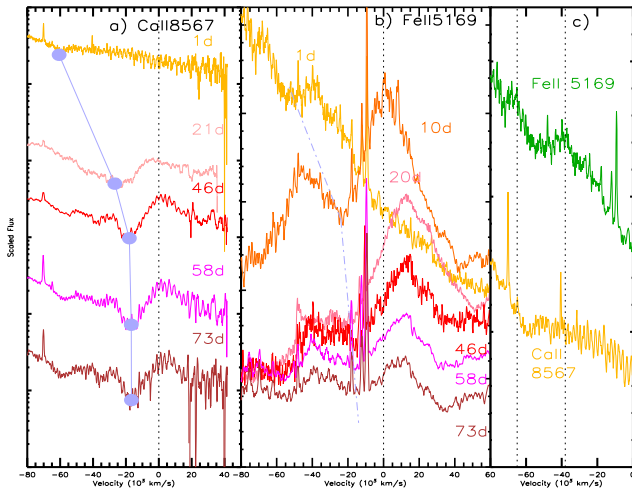


Figure 13. Velocity profiles and temporal evolution of IR Ca II line (panel (a)) at 8567 Å and Fe II at 5169 Å (panel (b)) in SN 2020bvc. Color-coding (panels (a) and (b)) is as in Figure 6. The absorption minima of Ca II are at velocities $-60,600$, $-26,800$, $-17,900$, $-16,800$, and $-16,700$ km s $^{-1}$ for days 1, 21, 46, 58, and 73, respectively. The temporal changes of the Fe II $\lambda 5169$ velocity are shown in Figure 14. (c) Zoomed-in version of velocity profiles of the 8567 Å Ca II (yellow) and Fe II at 5169 Å (green) showing absorption features at similar velocity. The dotted lines are at velocities of $-65,000$ and $-38,000$ km s $^{-1}$.

optical spectrum at day 3 in Figures 12(a) and (c). The optical spectra in Figure 12(b) confirm this trend. Since the optical spectra have a denser time sampling, they further constrain the steepness of velocity change to be maximum at day 12, which corresponds to the brightness peak (V_{\max}).

4.2.2. Type Ic-BL SN 2020bvc: Ca II and Fe II Velocities

SN Ic-BL are classified by their broad lines and high expansion velocities (i.e., 15,000 to 25,000 km s $^{-1}$ at maximum light; Modjaz et al. 2016) compared to those of normal SNe Ic. SNe Ic-BL are the only SN type associated with GRBs (Woosley & Bloom 2006; Modjaz 2011; Cano et al. 2017), indicating that their jet may be the origins of the high ejecta velocities (Barnes et al. 2018). When their jets fail to break out of the progenitors’ envelopes, they can release sufficient energy to produce the high expansion velocities characteristic of SNe Ic-BL (Lazzati et al. 2012). However, not all SNe Ic-BL are associated with observed GRBs. It is an open question as to whether there are different progenitor/explosion scenarios, or if the GRBs are sometimes simply missed owing to their being off-axis, or undetected owing to sensitivity limitations (see Modjaz et al. 2016, and references therein).

We have used the IR Ca II triplet absorption to determine the expansion velocities of SN 2020bvc, as we have done for SN 2020oi. SN 2020bvc shows a higher velocity change between days 1 and 20 than at later times. The first optical spectrum (day 1) shows an absorption centered at ~ 6850 Å (see Figure 6), which corresponds to an expansion velocity of $\sim 60,000$ km s $^{-1}$ for the Ca II triplets at 8567 Å (see Figure 13c). The temporal evolution of the triplet is shown in Figure 13(a). The change in velocity between days 1 and 20 is $\sim 34,000$ km s $^{-1}$, while from day 20 to 73 it is $\sim 10,000$ km s $^{-1}$. Such high expansion velocities in SN 2020bvc have also been reported by Izzo et al. (2020) and Ho et al. (2020c), using the Ca II triplet absorption feature in the same FLOYDS

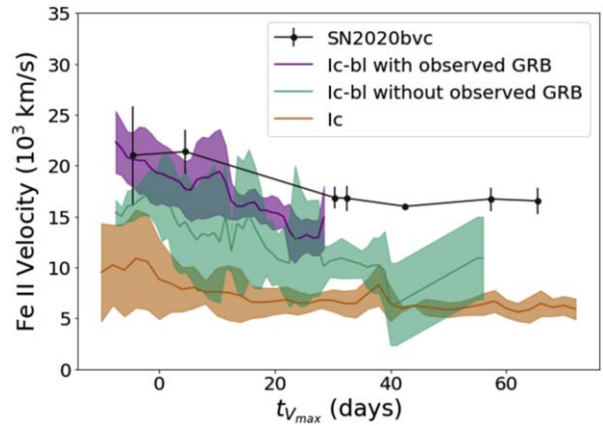


Figure 14. Fe II $\lambda 5169$ absorption velocity in SN 2020bvc (black) compared to the weighted mean velocities of SNe Ic (red), SNe Ic-BL with GRBs (purple), and SNe Ic-BL without observed GRBs (green), from Modjaz et al. (2016), measured in the same way as for SN 2020bvc. Time $t_{V_{\max}}$ ($=t_0 - 16.3$) is measured relative to date of max in the V band. The high velocities of SN 2020bvc are more consistent with those of SNe Ic-BL associated with GRBs, indicating that the on-axis-unobserved GRB model may be more appropriate for SN 2020bvc.

spectrum (available in TNS) on day 1. Significant velocity changes in eight optical spectra taken during the pre-max stage are also shown by Ho et al. (2020c), who report the change of 32,000 km s $^{-1}$ in expansion velocity between days 0.76 and 12.5. Their results are consistent with our findings. The separation between the absorption minimum and the emission peak of the Ca II triplet in SN 2020bvc is about 13,000–15,000 km s $^{-1}$ at late times, which is comparable to that in the Type Ic SN 2020oi. The blueshifted lines indicate high velocities, up to 60,000 km s $^{-1}$ for SN 2020bvc and 20,000 km s $^{-1}$ for SN 2020oi, and the expansion velocity rapidly declines before the optical maximum. After the optical maximum (e.g., V_{\max}), the velocity slowly declines in both SNe.

The temporal changes of the velocity profiles from the absorption minima of 5169 Å Fe II are shown in Figure 13(b). The optical spectrum at 10 days includes this Fe II line. The evolution of the profile is similar to that of the Ca II feature. We measured the velocity of the blended Fe II $\lambda 5169$ absorption line of SN 2020bvc using the method developed by Modjaz et al. (2016), which uses emcee (Foreman-Mackey et al. 2013), a Monte Carlo Markov Chain sampler, and accounts for both blueshift and broadening of the lines. The high velocities derived from Fe II lines shown in Figure 14 are in good agreement with those from the Ca II triplet in Figure 13(a). Figure 14 shows the temporal changes in the Fe II $\lambda 5169$ absorption velocities in SN 2020bvc and compares them with a large sample of SNe Ic-BL (Modjaz et al. 2016). The high velocities of SN 2020bvc are in better agreement with those SNe Ic-BL associated with GRBs than those with Type Ic-BL without associated GRBs. If SNe Ic-BL without associated GRBs are off-axis GRBs, our results indicate that the on-axis-unobserved GRB scenario is more appropriate for SN 2020bvc, which is supported by the work by Ho et al. (2020a). In contrast, Izzo et al. (2020) suggest an off-axis GRB for SN 2020bvc because of the lack of early X-ray detection. Based on the analysis of the expansion velocity in SN 2020bvc, we favor an on-axis-unobserved GRB over an off-axis GRB scenario.

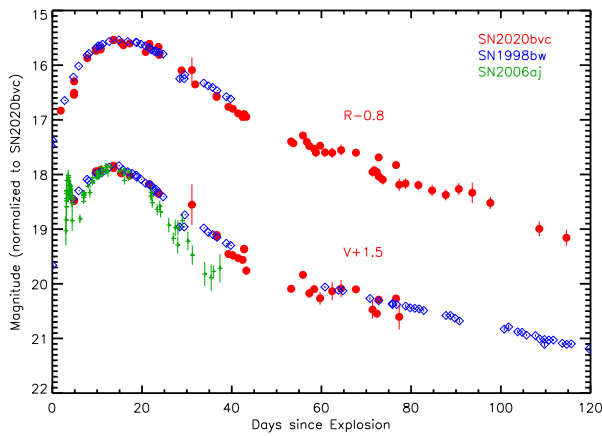


Figure 15. Optical light curve of SN 2020bvc in V and R bands compared with SN 1998bw and SN 2006aj. The light curves of the two comparison SNe are scaled to match those of SN 2020bvc at its peaks.

4.3. SN 2020bvc Light Curves and Their Implication

The light curves of SN 2020bvc in the V and R bands are compared with SN 1998bw and SN 2006aj in Figure 15, and their progenitor and explosion parameters are compared in Table 2. The light curves of SN 2020bvc at V and R have early bright peaks as shown in Figure 5 (see Ho et al. 2020c). Such early first peaks are not usually found in SNe Ic-BL (SN 2006aj shows a similar first peak in V). The overall SN parameters (energy, ejecta mass, and nickel mass) of SN 2020bvc are comparable to those of SN 1998bw, and the light curves of SN 2020bvc are similar to those of SN 1998bw. The light curve of SN 2006aj shows a more rapid decline following the peak than either SN 2020bvc or SN 1998bw.

Our best-fit model parameters for SN 2020bvc ($E_K = 1.1 \times 10^{52}$ erg, $M_{ej} = 6.36 M_\odot$, $M_{Ni} = 0.4 M_\odot$) are comparable to SN 1998bw, in general ($M_{ej} \sim 6.8$, $M_{Ni} \sim 0.4$, $E_K \sim 2 \times 10^{52}$ erg; e.g., Cano 2013; see Table 2). The nickel mass largely determines the peak brightness and does not sensitively depend on the ejecta mass and energy, assuming that there is no other power source such as a magnetar (Maeda et al. 2007). The energy and ejecta mass, together with the nickel mass determined from the peak luminosity, give the width of the light curve. A degeneracy exists between E_K , and M_{ej} , and thus our model is not a unique solution. For example, the light curve of SN 2020bvc might also be explained by a smaller ejecta mass and energy for the same nickel mass.

In a test model, we have applied the SN parameters (see Table 2) derived by Ho et al. (2020c), who give a smaller explosion energy and ejecta and nickel masses (i.e., $E_{exp} = 3 \times 10^{51}$ erg, $M_{ej} = 1.0 M_\odot$, and $M_{Ni} = 0.11 M_\odot$). We find that in all bands and all times the light resulting from Ho’s parameters is much fainter than the observed light curves. The Ni mass of $0.11 M_\odot$ is too small to explain the observed optical brightness where the difference is up to 1.5 mag. The ejecta mass of $1.0 M_\odot$ and the energy of 3×10^{51} erg result in too narrow light curves to explain the broad light curve.

There are only about a dozen published stripped SNe (i.e., SNe of Types IIb, Ib, Ic, and Ic-BL) that show double-peak light curves (see Figure 4 of Modjaz et al. 2019). As we have modeled the light curves of SN 2020bvc, the interaction with an extended CSM shell around the progenitor (e.g., Piro 2015) can reproduce the first peak, which is caused by shock cooling emission of the CSM heated by the SN shock. Our estimated CSM mass

$M_{CSM} = 0.1 M_\odot$ within the region of $R_{CSM} = 10^{14}$ cm implies that the progenitor experienced a mass eruption with $\dot{M} \sim 1.0 (v_w/100 [\text{km s}^{-1}]) M_\odot \text{ yr}^{-1}$ shortly before the SN explosion (i.e., $t < 1.0$ yr) with the CSM material in a confined region ($\sim 10^{14}$ cm). This high mass-loss rate is difficult to reconcile with the previously suggested scenarios for pre-SN mass loss from stripped-envelope SN progenitors (e.g., Aguilera-Dena et al. 2018; Fuller & Ro 2018). A luminous blue variable (LBV) star’s present-day mass-loss rate is typically about $10^{-3} M_\odot \text{ yr}^{-1}$. However, during a certain time period of Eta Carinae, the mass-loss rate was much higher, at about $1 M_\odot \text{ yr}^{-1}$ (Smith et al. 2003; Smith & Ferland 2007), which is approximately the same order of magnitude as the inferred high mass-loss rate in SN 2020bvc.

There are two other possible scenarios to explain the bright first peak. It might result from an expansion of the progenitor’s outer region during the pre-SN stage due to an energy injection from the inner convective layers (Fuller & Ro 2018). Ho et al. (2020c) suggest that the first peak is due to shock cooling emission (Nakar & Piro 2014) from extended low-mass material (mass $M < 10^{-2} M_\odot$ at radius $R > 10^{12}$ cm). Alternatively, the first peak may be caused by the interaction with a binary companion, similar to the case of SNe Ia (Kasen 2010). A more precise determination of SN parameters would require an exploration of the full parameter space, which is outside of this paper’s scope and will be the subject of future work. SN 2020bvc is a valuable addition to the sample of SNe with double peaks.

4.4. SN 2020oi Classification and Helium

SN 2020oi is classified as Type Ic based on the absence of hydrogen features in its spectra and the lack of strong helium lines typical of an SN Ib. The distinction between SNe Ic and SNe Ib is based on the presence of helium. However, helium may be hidden in SNe Ib, and the difference may be to what extent radioactive nickel is sufficiently mixed into the He layers (Wheeler et al. 1987). In order to compare SN 2020oi to the SN Ic population to understand how “typical” it is, we compare its spectra at multiple phases with the SN Ic mean spectral templates produced by Liu et al. (2016).

In the SN 2020oi spectra, we examined absorption features that could be consistent with He I $\lambda 5875$ and $1.0831 \mu\text{m}$. However, these lines are commonly contaminated with Na I D and S I, respectively. The IR He I line at $2.0587 \mu\text{m}$ is a much more precise indicator of He abundance in SN ejecta (Chugai 1990; Patat et al. 2001; Modjaz et al. 2009). With the assumption that the spectral features near the wavelength of this line are indeed produced by He I, we present velocity profiles of the line in Figure 12(d). The profiles are consistent with an absorption line at an expansion velocity of $\approx 10,000 \text{ km s}^{-1}$, which is typical of the Ca II and S I, as shown in Figure 12, although the putative He I absorption trough is not as strong as in bona fide SNe Ib (e.g., SN 2008D; see Figure 14 of Modjaz et al. 2009). Figure 12(d) hints at temporal changes of the velocities of He I. The optical He I $\lambda 5875$ line profile also is consistent, with a similar expansion velocity after day 12 in Figure 6 (this He line is marked on the spectrum on day 49 in Figure 17).

To classify SN 2020oi, we have applied the principal component and support vector machine method (see Williamson et al. 2019, for details). The results are shown in Figure 16. We find that SN 2020oi is consistent with the SN Ic population

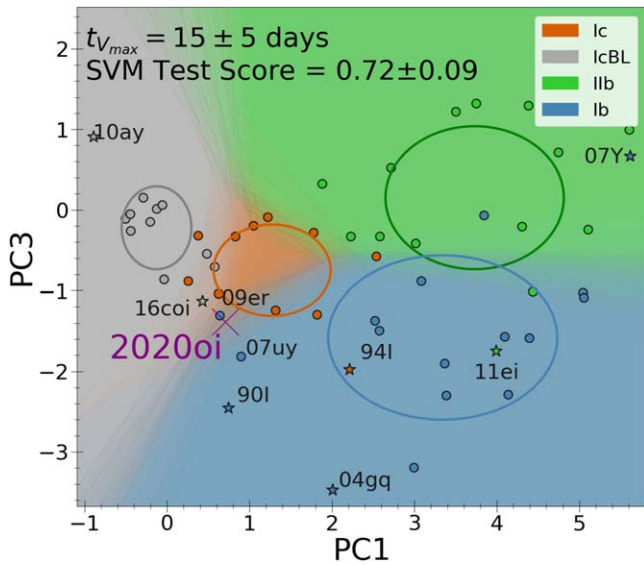


Figure 16. Classification of SN 2020oi (purple cross) is shown in the phase space presented in Williamson et al. (2019). PC1 (Principle Component 1) and PC3 are principle component decompositions from the mean spectra of many SNe Ic over 0–5 days after $t_{V(\max)}$ and 5–15 days, respectively. The colored regions are determined by a support vector machine trained on a principal component decomposition of a stripped-envelope SN data set. Ellipses mark the regions within one standard deviation for each subtype. SNe that are two standard deviation outliers are marked with stars and labeled. SN 2020oi is located between the SN Ic (red) and SN Ib (blue) regions.

at the 1σ level, but that it is near the boundary between the SN Ic (red) and SN Ib (blue) regions. In particular, two of the top five spectral matches (matches are nearest neighbor spectra in the principle component analysis [PCA] phase space) are the peculiar SNe Ib SN 2007uy and SN 2009er. These two SNe have weaker He lines than the typical SNe Ib (Modjaz et al. 2014), along with broader features at higher velocities than the typical SN Ib.

It is challenging to confidently identify the lines (and infer abundances) in stripped-envelope SNe without full radiative transfer simulations because of the large line shifts caused by high expansion velocities. Multiple groups have produced synthetic models of SN Ic spectra, including ones with small amounts of He (i.e., $<0.1 M_{\odot}$) that are consistent with observations (Dessart et al. 2012; Hachinger et al. 2012; M. Williamson et al. 2020, in preparation). However, so far, the synthetic spectral models of SNe have been limited to optical spectra. Expanding the wavelength coverage to the NIR should allow most of the observed atomic lines. However, including molecule formation, and possibly including a dust model, would be required to reproduce the CO features and the rising K -band continuum such as is seen in SN 2020oi at day 63 (see Figure 7). Efforts in at least some of those directions will be the focus of future research.

4.5. Spectral Evolution and Comparison with Other SNe

4.5.1. Type Ic SN 2020oi

In Figure 17 the spectra of SN 2020oi are compared with two other SNe Ic, SN 2007gr and SN 1994I, and those of SN 2020bvc with two SNe Ic-BL, SN 1998bw and SN 2006aj. Here the day numbers for each spectrum at right in the figure are days after the maximum light (e.g., in B band for SN 2007gr; Hunter et al. 2009). To make the number of days

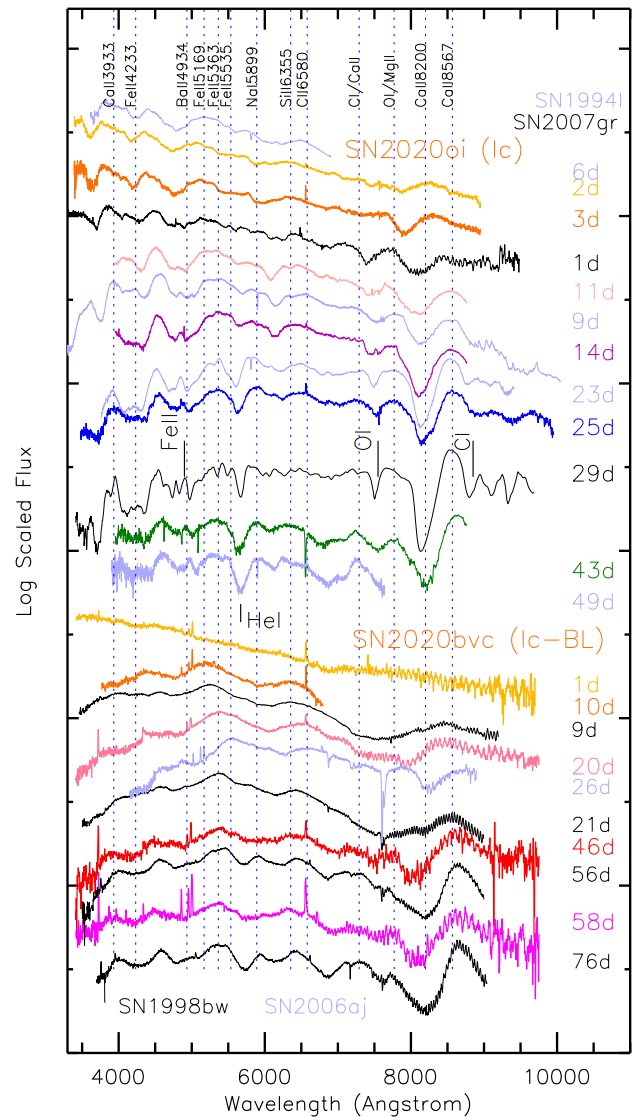


Figure 17. Upper half: optical spectra of SN 2020oi compared with SN 2007gr (in black) and SN 1994I (in light blue). Lower half: optical spectra of SN 2020bvc are with SN 1998bw (in black) and SN 2006aj (in light blue). The colors of SN 2020oi and SN 2020bvc are the same as those in Figure 6. The numbers on the right side are approximately the days since the explosion. The locations of optical He I, Fe II, O I, and C I lines are marked in the middle, and the order of the spectra is in the numbers.

compared to those in SN 2020oi, we added 11.5 days from the B_{\max} day, which was an approximation.

Overall the spectra of SN 2020oi are similar to those of SN 2007gr, but at later epochs (>25 days), SN 2020oi has weaker lines than SN 2007, including those of Fe (around $\sim 4800 \text{ \AA}$), O I (at 7774 \AA), and C I (at 8727 \AA), marked on the spectra of day 29 in Figure 17. The progenitor parameters derived from the light curves also show that SN 2020oi has an ejecta mass of $0.71 M_{\odot}$, lower than the $2\text{--}3 M_{\odot}$ for SN 2007gr (see Table 2), although the Ni masses of both SNe are $\sim 0.07 M_{\odot}$. Strong Fe lines in optical band are suggested to be due to Fe clumping (Mazzali et al. 2010).

The four SN 1994I spectra shown in Figure 17 are remarkably similar to those of SN 2020oi except for a slight difference in velocity shifts. However, after day 40, the velocities are comparable. The spectra between SN 2020oi at day 25 are very similar to those of SN 1994I at day 23 except

for the strength of the Na I D line caused by different amounts of interstellar gas on their sight lines. This confirms the finding of similarity between SN 2020oi and SN 1994I from the light curves in Section 3.2 and the CO emission analysis in Section 4.1. SN 1994I has commonly been considered a standard example of Type Ic. SN 2020oi is the second such standard example. We encourage the development of more comprehensive hydrodynamical models in order to create a rich set of model spectra for future studies of elemental abundances and mixing.

4.5.2. Type IC-BL SN 2020bvc

Figure 17 shows that the spectra of SN 2020bvc are similar to those of another SN Ic-BL, SN 1998bw. In particular, the spectrum at day 20 of SN 2020bvc is nearly identical to that of SN 1998bw at day 21, including the peaks of the Fe II and Ca II absorption features. SN 1998bw shows a $\sim 35,000 \text{ km s}^{-1}$ blueshifted line, similar to what is observed in SN 2020bvc. In SN 1998bw, at the intermediate phase between photospheric and fully nebular phase, the expansion velocities ($\sim 10^4 \text{ km s}^{-1}$) remained exceptionally high compared to those of other recorded CCSNe at similar phases (Patat et al. 2001). The velocity change in SN 2020bvc is also $\sim 10,000 \text{ km s}^{-1}$, again comparable to those in SN 1998bw. However, after day 20, while the spectral shape of SN 2020bvc remains unchanged, SN 1998bw shows noticeable changes in its spectra; some lines become more prominent, while the widths of the main lines become narrower. The line broadening remains in SN 2020bvc the same (about $\sim 20,000 \text{ km s}^{-1}$) until our final spectrum at day 73. In SN 1998bw, more lines appeared, including nebular lines, which became noticeable from day 51 (see spectra at days 56 and 76 in Figure 17). The spectrum of SN 1998bw became more similar to typical Type Ic at later times, but this is not the case for SN 2020bvc, as shown in Figure 17. The properties of the explosion and the progenitor derived for SN 2020bvc and SN 1998bw are comparable; both have an explosion energy of 10^{52} erg. There are some additional differences between the two SNe, though. Some He weak lines in SN 1998bw are identified (Patat et al. 2001), while the presence of He lines in SN 2020bvc is unclear. Most importantly, SN 2020bvc does not have an identified γ -ray counterpart so far, whereas SN 1998bw is coincident with GRB 980425. According to Woosley et al. (1999), its γ -ray emission is due to shock breakout and relativistic shock deceleration in circumstellar material in a highly asymmetric explosion.

The spectral comparison between SN 2020bvc (day 20) and SN 2006aj (day 26) in Figure 17 shows that they have similar broadened line patterns (the widths of the lines are comparable). Interestingly, the blueshifts in SN 2006aj are much smaller than those of SN 2020bvc. Optical spectra of SN 2006aj do not show high-velocity lines such as the ones in SN 2020bvc (Modjaz et al. 2006; Waxman et al. 2007).

The light curve and spectral comparison described above show that SN 2020bvc is more similar to SN 1998bw than SN 2006aj. Thus, our results suggest that the explosion and progenitor parameters of SN 2020bvc and SN 1998bw are different from SN 2006aj (Table 2) with larger explosion energies, progenitor stars, and Ni masses.

The temporal behaviors of the spectral shape and line profiles in SN 2020bvc are very similar to those of Type Ic-BL SN 1998bw. Our findings that SN 2020bvc and SN 1998bw have very similar light curves, explosion parameters, and high

expansion velocities, while the nearby SN 1998bw had an observed GRB of very low luminosity, are consistent with the suggestion by Ho et al. (2020c) that SN 2020bvc may also have had an associated GRB that was not found by GRB satellites.

5. Conclusion

1. We have presented NIR and optical observations of the Type Ic SN 2020oi in the galaxy M100 and the broad-lined Type Ic SN 2020bvc in UGC 09379, using Gemini, LCO, SOAR, and other ground-based telescopes. The light curves of SN 2020oi cover ~ 100 days after the explosion and for 80 days after the explosion for SN 2020bvc. We present an analysis of 13 optical spectra and 4 NIR spectra of SN 2020oi and 8 optical spectra and 1 NIR spectrum of SN 2020bvc. These two explosions provide a rare opportunity to compare their temporal and spectral evolutions of SNe Ic and SNe Ic-BL. The spectra of both SN 2020oi and SN 2020bvc exhibit dominant emission lines from Fe II, Si II, Ca II, C I, S I, and Si I.

2. The light curves of SN 2020oi show a gradual increase over the first 10 days since the explosion and a rapid decrease over 25 days. At later times the light curves show slight decreases. Calculations performed using the one-dimensional multigroup radiation hydrodynamics code STELLA imply that SN 2020oi has a canonical explosion energy, an Ni mass of $0.07 M_{\odot}$, and an ejecta mass of $0.7 M_{\odot}$ and is remarkably similar to SN 1994I.

3. In the Type Ic SN 2020oi, CO emission is detected at day 63. The CO emission profile is featureless, presumably due to the emission occurring over a wide velocity range. The CO emission appears to be in transition from the optically thick to the optically thin regime, the latter phase allowing more effective cooling of the deeper, dense layers. The CO mass is greater than $10^{-3} M_{\odot}$, and the CO temperature is 3000–3300 K; a fully mixed model is required to reproduce the observed CO features.

4. The NIR spectrum of SN 2020oi at day 63 also reveals a rising continuum in the *K* band, which must be due to emission by heated dust, at a temperature of ~ 800 K and a mass of $10^{-5} M_{\odot}$. This is the first detection of dust in an SN Ic. We explore scenarios for creating dust in the SN ejecta or in the CSM and heating preexisting CSM dust or emission via an infrared echo as explanations of the rising continuum. The fact that the observed dust temperature is consistent with the equilibrium dust temperature from the SN raises the possibility that the rising continuum can come from newly formed dust either in the ejecta or in circumstellar knots. However, heated dust from a circumstellar shell or an IR echo is still a plausible explanation for the rising continuum.

5. A new STELLA SN model consisting of a helium-poor CO star of $M = 8.26 M_{\odot}$, corresponding to an initial mass of $40\text{--}50 M_{\odot}$, explosion energy of $E_{\text{exp}} = 12 \times 10^{51}$ erg, and radioactive nickel mass of $0.4 M_{\odot}$, produces a reasonably good fit for the main peak and the light curves of SN 2020bvc. The Ni in the SN is assumed to be uniformly mixed. A model with the progenitor surrounded by massive CSM can reproduce the first peak of the light curves. The light curve and explosion parameters are similar to SN 1998bw.

6. Temporal changes of the blueshifted absorption lines, which are most noticeable in the NIR Ca II triplet and Si II lines, are observed in both SN 2020oi and SN 2020bvc. These blueshifted absorptions are at high velocities, up to

60,000 km s⁻¹ for SN 2020bvc and 20,000 km s⁻¹ for SN 2020oi during pre-maximum. The expansion velocities thereafter decrease to $\sim 6000\text{--}10,000$ km s⁻¹ in both SNe. The overall shape of the SN 2020bvc spectrum after day 20 remains surprisingly unchanged up to day 73. The temporal behavior of SN 2020bvc in terms of spectral shape and line profiles is very similar to that of Type Ic-BL SN 1998bw.

7. We show a potential helium absorption in the SN 2020oi spectra. However, our PCA analysis, compared with many other SNe Ic, shows that SN 2020oi is still consistent with the SN Ic population.

We thank an anonymous referee for helpful comments and suggestions, which helped to improve the paper. J.R. thanks Nathan Smith for the helpful discussion on Eta Carina and Bill Reach on the dust grain temperature. This paper is based in part on observations obtained at the international Gemini Observatory, a program of NSF OIR Lab, which is managed by the Association of Universities for Research in Astronomy (AURA) under a cooperative agreement with the National Science Foundation on behalf of the Gemini Observatory partnership: the National Science Foundation (United States), National Research Council (Canada), Agencia Nacional de Investigación y Desarrollo (Chile), Ministerio de Ciencia, Tecnología e Innovación (Argentina), Ministério da Ciência, Tecnologia, Inovações e Comunicações (Brazil), and Korea Astronomy and Space Science Institute (Republic of Korea); and based in part on observations obtained at the Southern Astrophysical Research (SOAR) telescope, which is a joint project of the Ministério da Ciência, Tecnologia e Inovações (MCTI/LNA) do Brasil, the US National Science Foundations NOIRLab, the University of North Carolina at Chapel Hill (UNC), and Michigan State University (MSU). This work makes use of observations obtained with the Las Cumbres Observatory network.

J.R. acknowledges support from NASA ADAP grant (80NSSC20K0449) and various Guest Observer Programs for the study of SN dust. D.A.H., C.M., J.B., and D.H. are supported by NASA grants 80NSSC19k1639 NSF AST-1911225 and AST-1911151. S.V. is supported by NSF AST-1813176. D.P.K.B. is supported by a CSIR Emeritus Scientist grant-in-aid, which is being hosted by the Physical Research Laboratory, Ahmedabad. P.H. acknowledges support by the National Science Foundation (NSF) grant (AST-1008962). S.-C.Y. is supported by the National Research Foundation of Korea (NRF) grant (NRF-2019R1A2C2010885). L.G. was funded by the European Union’s Horizon 2020 research and innovation program under the Marie Skłodowska-Curie grant agreement No. 839090. This work has been partially supported by the Spanish grant PGC2018-095317-B-C21 within the European Funds for Regional Development (FEDER). H.A. acknowledges support from the Basic Science Research Program through the National Research Foundation of Korea (NRF) funded by the Ministry of Science, ICT & Future Planning (NRF-2017R1C1B2004566). M.M. and the SNYU group are supported by the NSF CAREER award AST-1352405 and by a Humboldt Faculty Fellowship. J.V. and his group at Konkoly Observatory are supported by the project “Transient Astrophysical Objects” GINOP 2.3.2-15-2016-00033 of the National Research, Development and Innovation Office (NKFIH), Hungary, funded by the European Union and partly by the KEP-7/2018 grant of the Hungarian Academy

of Sciences. K.V. and L.K. received support from the NKFIH/OTKA grants KH-130526 and K-131508. K.V. also acknowledges the partial support from the Lendület Program of the Hungarian Academy of Sciences, project No. LP2018-7/2019. We thank participating observers on the UW APO ZTF follow-up team, including Brigitta Spíócz, Eric Bellm, Zach Golkhou, Keaton Bell, and James Davenport. M.L.G. acknowledges support from the DiRAC Institute in the Department of Astronomy at the University of Washington. The DiRAC Institute is supported through generous gifts from the Charles and Lisa Simonyi Fund for Arts and Sciences and the Washington Research Foundation.

Software: Figaro (Shortridge et al. 1992), Gemini IRAF Package, lcgtsnpipe (Valenti et al. 2016), PyZOGY (Guevel & Hosseinzadeh 2017), IRAF (Tody 1986, 1993), FLOYDS pipeline (Valenti et al. 2014), PyDIS (Davenport 2018), STELLA (Blinnikov et al. 2000, 2006), MPFIT (Markwardt 2009), Spextool (Cushing et al. 2004).

Appendix Diagnostics and Sensitivities of Molecular Bands

In this appendix, we demonstrate the diagnostics and their sense of observational signatures for conditions and abundances found in SNe Ic, i.e., C/O/Si-rich mixtures. We assume a thermal radiation field and neglect time dependence of the formation because it will change the flux but hardly the opacity profiles. This allows linking results from SN 2020oi to many future SNe of CCSNe with ground-based NIR and MIR observations such as JWST.

For the dependence of the density and velocity dispersion, we refer to studies cited in Section 4.1.2. In Figure 18, we demonstrate the sensitivity of the temperature, abundances for (C/O/Si)-rich compositions with abundance ratios of (1:1:0) and (1:2:1), a particle abundance of 5×10^{11} cm⁻³, and a velocity dispersion of 1000 km s⁻¹ typically found in SNe Ic envelopes. The influence of nonthermal ionization by radioactive decay is parameterized by the ⁺CO/CO ratio.

In the NIR and for temperatures T below 5000 K, the opacities of the first CO and CO⁺ overtones decrease rapidly with T and, under SN Ic conditions, produce optically thick features. Below $T \leq 2000$ K, the first and second vibrational modes dominate (Figure 18). Note that the second vibrational mode is strong because of its statistical weight.

Nonthermal excitation has three signatures in the NIR: (a) CO⁺ adds a blueshifted emission component, (b) the peak of the emission rises to the third component in the spectra even at low T , and (c) the appearance of a strong second overtone. Signatures (b) and (c) can be used to detect or constrain the amount of mixing in SNe Ic. Note that signature (c) requires good signal-to-noise ratio (S/N) spectra, but it is not sensitive to inhomogeneities and large asphericity effects expected in SNe Ib/c (see above). Moreover, ground-based NIR spectra allow for significantly better S/N in the H band compared to the K band. In practice, a problem during the semi-transparent phase is line blending by allowed transitions that are produced in the region inside the CO-forming region but dominate the spectra until the nebular phase.³³ Moreover, the wide wavelength range spans from the J to the H band range, making pattern recognition of the different modes problematic for ground-based observations.

³³ By pattern recognition algorithms, the signatures may be recovered, though.

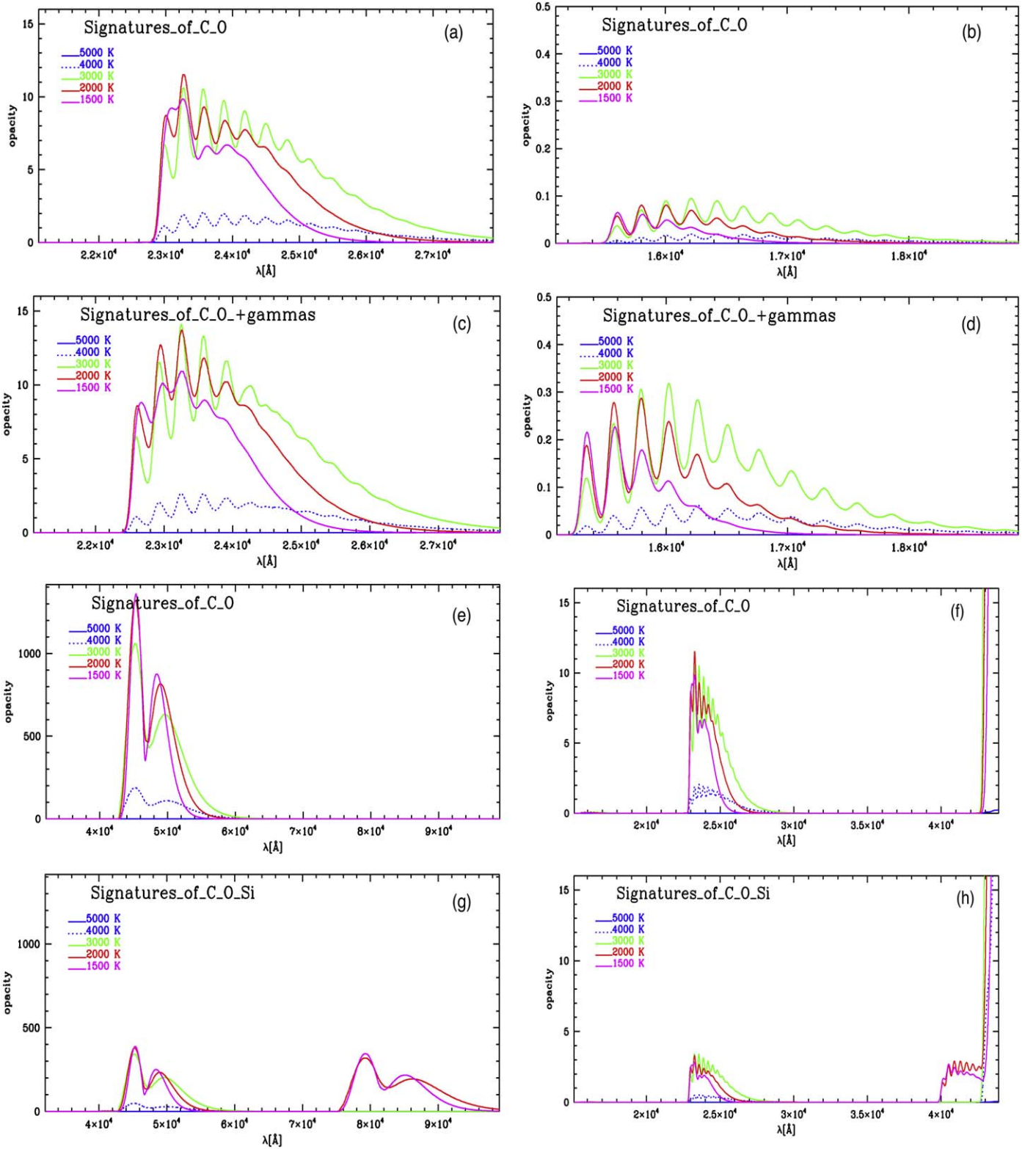


Figure 18. NIR and MIR (1.4–10 μm) spectral signatures of the fundamental, first, and second vibrational bands of CO, CO⁺, and SiO for the C/O layer (panels (a)–(f)) and the C/O/Si-rich layer with equal C and Si abundances (panels (g)–(h)), and for a velocity dispersion of 1000 km s^{−1}. All simulations include CO, CO⁺, and SiO. In each panel the temperature dependence of the spectral features is shown. (a–d) Effect of nonthermal excitation on the first (panels (a) and (c)) and second overtone (panels (b) and (d)) of CO and CO⁺ without (panels (a) and (b)) and with (panels (c) and (d)) nonthermal excitation. (e–h) Spectral signatures due to the effect of the abundances. The fundamental CO (panel (e)) and first-overtone CO (panel (f)) bands dominate for CO-rich layers, but, in addition, the fundamental SiO (panel (g)) and first-overtone SiO (panel (h)) bands start to emerge for C/O/Si layers (the second overtone of SiO at $\sim 28,000$ Å is too faint to appear). Nonthermal excitation and ionization have been neglected in all models, but for those in panels (c) and (d) we assumed CO⁺/CO = 1. Note that nonthermal excitation with long recombination and charge-exchange timescales will produce a strong second CO overtone in the NIR, and, for temperature ≤ 2000 K, the first SiO overtone produces a “wing” on the short-wavelength edge of the fundamental CO band (panel (h)) comparable in strength to the first overtone of CO. For more details see the text.

The MIR molecule spectra are dominated by the fundamental CO band. The large opacity allows for detailed studies of the onset of CO formation to become optically thick in SNe Ibc with the exception of the high overtones. Thus, MIR observations should cover a wide wavelength range. The change of the opacity profile can be understood in the same way as the overtone bands.

For $T \leq 2000$ K one may expect to see the fundamental band of SiO if the photosphere has receded to the corresponding layers in a massive stellar explosion, or if large asymmetric explosions “squeezed out” Si as described above. The appearance of an SiO band is a clear indication of low T at the inner layers, but its nonappearance does not imply the lack of large- or small-scale mixing. Note that the fundamental SiO bands may have been observed in the SN 1998S with the Spitzer Space Telescope, though, unfortunately, the spectra have been hampered by the order overlap and possibly calibration issues at the red wing (Gerardy et al. 2002).

At low T , the first SiO overtone is clearly present in compositions with more O than C. It is a probe for large- versus small-scale mixing processes at work. In our example (Figure 18, bottom right panel), its strength is comparable to the first CO overtone, which allows the analysis based on its profile. However, it provides a sensitive temperature indicator for values close to the dust formation temperature.

ORCID iDs

J. Rho  <https://orcid.org/0000-0003-3643-839X>
 A. Evans  <https://orcid.org/0000-0002-3142-8953>
 T. R. Geballe  <https://orcid.org/0000-0003-2824-3875>
 P. Hoeflich  <https://orcid.org/0000-0002-4338-6586>
 M. Shahbandeh  <https://orcid.org/0000-0002-9301-5302>
 S. Valenti  <https://orcid.org/0000-0001-8818-0795>
 S.-C. Yoon  <https://orcid.org/0000-0002-5847-8096>
 M. Williamson  <https://orcid.org/0000-0003-2544-4516>
 M. Modjaz  <https://orcid.org/0000-0001-7132-0333>
 D. Hiramatsu  <https://orcid.org/0000-0002-1125-9187>
 C. Pellegrino  <https://orcid.org/0000-0002-7472-1279>
 J. Vinkó  <https://orcid.org/0000-0001-8764-7832>
 C. McCully  <https://orcid.org/0000-0001-5807-7893>
 T. Pritchard  <https://orcid.org/0000-0001-9227-8349>
 J. Andrews  <https://orcid.org/0000-0003-0123-0062>
 L. Galbany  <https://orcid.org/0000-0002-1296-6887>
 S. Van Dyk  <https://orcid.org/0000-0001-9038-9950>
 M. L. Graham  <https://orcid.org/0000-0002-9154-3136>
 S. Blinnikov  <https://orcid.org/0000-0002-5726-538X>
 V. Joshi  <https://orcid.org/0000-0002-1457-4027>
 A. Pál  <https://orcid.org/0000-0001-5449-2467>
 R. Szakats  <https://orcid.org/0000-0002-1698-605X>
 K. Vida  <https://orcid.org/0000-0002-6471-8607>

References

Aguilera-Dena, D. R., Langer, N., Moriya, T. J., & Schootemeijer, A. 2018, *ApJ*, 858, 115
 Andrews, J. E., Clayton, G. C., Wesson, R., et al. 2011, *AJ*, 142, 45
 Arnett, W. D. 1982, *ApJ*, 253, 785
 Banerjee, D. P. K., Joshi, V., Evans, A., et al. 2018, *MNRAS*, 481, 806
 Banerjee, D. P. K., Srivastava, M. K., Ashok, N. M., & Venkataraman, V. 2016, *MNRAS*, 455, L109
 Barnes, J., Duffell, P. C., Liu, Y., et al. 2018, *ApJ*, 860, 38
 Bellm, E. C., Kulkarni, S. R., Graham, M. J., et al. 2019, *PASP*, 131, 018002
 Bertoldi, F., Carilli, C. L., Cox, P., et al. 2003, *A&A*, 406, L55

Bevan, A., Wesson, R., Barlow, M. J., et al. 2019, *MNRAS*, 485, 5192
 Bianco, F. B., Modjaz, M., Hicken, M., et al. 2014, *ApJS*, 213, 19
 Blinnikov, S., Lundqvist, P., Bartunov, O., Nomoto, K., & Iwamoto, K. 2000, *ApJ*, 532, 1132
 Blinnikov, S. I., Röpke, F. K., Sorokina, E. I., et al. 2006, *A&A*, 453, 229
 Bode, M. F., & Evans, A. 1980a, *A&A*, 89, 158
 Bode, M. F., & Evans, A. 1980b, *MNRAS*, 193, 21P
 Cano, Z. 2013, *MNRAS*, 434, 1098
 Cano, Z., Wang, S.-Q., Dai, Z.-G., & Wu, X.-F. 2017, *AdAst*, 2017, 1
 Chatzopoulos, E., Wheeler, J. C., & Vinko, J. 2012, *ApJ*, 746, 121
 Chawner, H., Marsh, K., Matsuura, M., et al. 2019, *MNRAS*, 483, 70
 Chugai, N. 1990, *SvA*, 34, 96
 Clemens, J. C., Crain, J. A., & Anderson, R. 2004, *Proc. SPIE*, 5492, 331
 Clocchiatti, A., & Wheeler, J. C. 1997, *ApJ*, 491, 375
 Couch, S. M. 2017, *RSPTA*, 375, 20160271
 Cushing, M. C., Vacca, W. D., & Rayner, J. T. 2004, *PASP*, 116, 362
 Das, R. K., Banerjee, D. P. K., & Ashok, N. M. 2009, *MNRAS*, 398, 375
 Davenport, J., de Val-Borro, M., & Wilkinson, T. D. 2018, PyDIS: Possibly Useful, <https://github.com/TheAstroFactory/pydis>, doi:10.5281/zenodo.58753
 De Looze, I., Barlow, M. J., Swinyard, B. M., et al. 2017, *MNRAS*, 465, 3309
 Dessart, L., Hillier, D. J., Li, C., & Woosley, S. 2012, *MNRAS*, 424, 2139
 Dessart, L., Hillier, D. J., Livne, E., et al. 2011, *MNRAS*, 414, 2985
 Dessart, L., Hillier, D. J., Woosley, S., et al. 2015, *MNRAS*, 453, 2189
 Di Carlo, E., Corsi, C., Arkharov, A. A., et al. 2008, *ApJ*, 684, 471
 Dominik, C. 1992, PhD thesis, Technische Universität
 Dominik, C., & Tielens, A. G. G. M. 1997, *ApJ*, 480, 647
 Drout, M. R., Milisavljevic, D., Parrent, J., et al. 2016, *ApJ*, 821, 57
 Dwek, E., & Arendt, R. G. 2008, *ApJ*, 685, 976
 Elmhamdi, A., Danziger, I. J., Cappellaro, E., et al. 2004, *A&A*, 426, 963
 Ergon, M., Sollerman, J., Fraser, M., et al. 2014, *A&A*, 562, A17
 Fan, Z., Wang, H., Jiang, X., et al. 2016, *PASP*, 128, 115005
 Fedkin, A. V., Meyer, B. S., & Grossman, L. 2010, *GeCoA*, 74, 3642
 Filippenko, A. V. 1982, *PASP*, 94, 715
 Filippenko, A. V. 1997, *ARA&A*, 35, 309
 Foreman-Mackey, D., Hogg, D. W., Lang, D., & Goodman, J. 2013, *PASP*, 125, 306
 Forster, F., Pignata, G., Bauer, F. E., et al. 2020, Transient Name Server Discovery Report, 2020-67, 1
 Fox, O. D., Chevalier, R. A., Dwek, E., et al. 2010, *ApJ*, 725, 1768
 Fryer, C. L., Mazzali, P. A., Prochaska, J., et al. 2007, *PASP*, 119, 1211
 Fuller, J., & Ro, S. 2018, *MNRAS*, 476, 1853
 Gall, C., Hjorth, J., Watson, D., et al. 2014, *Natur*, 511, 326
 Gal-Yam, A. 2017, *Observational and Physical Classification of Supernovae* (Berlin: Springer), 195
 Gerardy, C. L., Fesen, R. A., Höflich, P., & Wheeler, J. C. 2000, *AJ*, 119, 2968
 Gerardy, C. L., Fesen, R. A., Nomoto, K., et al. 2002, *PASJ*, 54, 905
 Gomez, H. L., Krause, O., Barlow, M. J., et al. 2012, *ApJ*, 760, 96
 Graham, J. R., & Meikle, W. P. S. 1986, *MNRAS*, 221, 789
 Grzegorzec, J. 2019, Transient Name Server Discovery Report, 2019-666, 1
 Guevel, D., & Hosseinzadeh, G. 2017, Dguevel/Pyzogy: Initial Release, v0.0.1, Zenodo, doi:10.5281/zenodo.1043973
 Hachinger, S., Mazzali, P. A., Taubenberger, S., et al. 2012, *MNRAS*, 422, 70
 Hiramatsu, D., Arcavi, I., Burke, J., et al. 2020, Transient Name Server Classification Report, 2020-403, 1
 Ho, A. Y., Kulkarni, S., Perley, D. A., et al. 2020a, *ApJ*, 902, 86
 Ho, A. Y. Q., Cenko, B., Perley, D., Corsi, A., & Brightman, M. 2020b, Transient Name Server AstroNote, 45, 1
 Ho, A. Y. Q., Kulkarni, S. R., Perley, D. A., et al. 2020c, *ApJ*, 902, 86
 Ho, A. Y. Q., Schulze, S., Perley, D., et al. 2020d, TNSAN, 8, 1
 Hoeflich, P., Ashall, C., Fisher, A., et al. 2019, in *Nuclei in the Cosmos XV*, Vol. 219 (Cham: Springer), 187
 Hoeflich, P., Nomoto, K., Umeda, H., & Wheeler, J. C. 2000, *ApJ*, 528, 590
 Hoeflich, P., Wheeler, J. C., & Wang, L. 1999, *ApJ*, 521, 179
 Hofflich, P., Langer, N., & Duschinger, M. 1993, *A&A*, 275, L29
 Hofflich, P., Sharp, C. M., & Zorec, J. 1989, in *Proc. of a Workshop, Particle Astrophysics: Forefront Experimental Issues*, ed. E. B. Norman (Singapore: World Scientific), 186
 Horesh, A., Sfaradi, I., Ergon, M., et al. 2020, *ApJ*, 903, 132
 Hubeny, I., & Lanz, T. 2003, in *ASP Conf. Ser. 288, Stellar Atmosphere Modeling*, ed. I. Hubeny, D. Mihalas, & K. Werner (San Francisco, CA: ASP), 51
 Hunter, D. J., Valenti, S., Kotak, R., et al. 2009, *A&A*, 508, 371
 Immler, S., Wilson, A. S., & Terashima, Y. 2002, *ApJL*, 573, L27
 Isaak, K. G., Priddey, R. S., McMahon, R. G., et al. 2002, *MNRAS*, 329, 149
 Iwamoto, K., Nomoto, K., Hoeflich, P., et al. 1994, *ApJL*, 437, L115

- Izzo, L., Auchettl, K., Hjorth, J., et al. 2020, *A&A*, 639, L11
- Jencson, J. E., Kasliwal, M. M., Johansson, J., et al. 2017, *ApJ*, 837, 167
- Joshi, V., Banerjee, D. P. K., & Srivastava, M. 2017, *ApJL*, 851, L30
- Kankare, E., Fraser, M., Ryder, S., et al. 2014, *A&A*, 572, A75
- Kasen, D. 2010, *ApJ*, 708, 1025
- Kasen, D., & Bildsten, L. 2010, *ApJ*, 717, 245
- Khokhlov, A. M., Hoefflich, P. A., Oran, E. S., et al. 1999, *ApJL*, 524, L107
- Kirchschlager, F., Schmidt, F. D., Barlow, M. J., et al. 2019, *MNRAS*, 489, 4465
- Kotak, R., Meikle, W. P. S., Farrah, D., et al. 2009, *ApJ*, 704, 306
- Kubát, J. 2009, in Proc. of the Int. Conf. in Honor of Dimitri Mihalas for His Lifetime Scientific Contributions on the Occasion of His 70th Birthday, Recent Directions in Astrophysical Quantitative Spectroscopy and Radiation Hydrodynamics (New York: AIP), 357
- Kumar, B., Singh, A., Srivastav, S., Sahu, D. K., & Anupama, G. C. 2018, *MNRAS*, 473, 3776
- Laporte, N., Ellis, R. S., Boone, F., et al. 2017, *ApJL*, 837, L21
- Lazzati, D., Morsony, B. J., Blackwell, C. H., & Begelman, M. C. 2012, *ApJ*, 750, 68
- Lepp, S., Dalgarno, A., & McCray, R. 1990, *ApJ*, 358, 262
- Leńniewska, A., & Michałowski, M. J. 2019, *A&A*, 624, L13
- Li, Z.-Y., & Chevalier, R. A. 1999, *ApJ*, 526, 716
- Liu, Y.-Q., Modjaz, M., Bianco, F. B., & Graur, O. 2016, *ApJ*, 827, 90
- Maeda, K., Tanaka, M., Nomoto, K., et al. 2007, *ApJ*, 666, 1069
- Markwardt, C. B. 2009, in ASP Conf. Ser. 411, Astronomical Data Analysis Software and Systems XVIII, ed. D. A. Bohlender, D. Durand, & P. Dowler (San Francisco, CA: ASP), 251
- Matsuura, M., Dwek, E., Barlow, M. J., et al. 2015, *ApJ*, 800, 50
- Maund, J. R., Wheeler, J. C., Patat, F., et al. 2007, *ApJ*, 671, 1944
- Mazzali, P. A., Deng, J., Nomoto, K., et al. 2006, *Natur*, 442, 1018
- Mazzali, P. A., Maurer, I., Valenti, S., Kotak, R., & Hunter, D. 2010, *MNRAS*, 408, 87
- Mazzali, P. A., Sullivan, M., Pian, E., Greiner, J., & Kann, D. A. 2016, *MNRAS*, 458, 3455
- Meikle, W. P. S., Spyromilio, J., Allen, D. A., Varani, G. F., & Cumming, R. J. 1993, *MNRAS*, 261, 535
- Micelotta, E. R., Dwek, E., & Slavin, J. D. 2016, *A&A*, 590, A65
- Michałowski, M. J. 2015, *A&A*, 577, A80
- Mihalas, D., Kunasz, P. B., & Hummer, D. G. 1975, *ApJ*, 202, 465
- Mihalas, D., & Mihalas, B. W. 1984, Foundations of Radiation Hydrodynamics (Oxford: Oxford Univ. Press), 731
- Modjaz, M. 2011, *AN*, 332, 434
- Modjaz, M., Blondin, S., Kirshner, R. P., et al. 2014, *AJ*, 147, 99
- Modjaz, M., Gutiérrez, C. P., & Arcavi, I. 2019, *Nature Astronomy*, 3, 717
- Modjaz, M., Li, W., Butler, N., et al. 2009, *ApJ*, 702, 226
- Modjaz, M., Liu, Y. Q., Bianco, F. B., & Graur, O. 2016, *ApJ*, 832, 108
- Modjaz, M., Stanek, K. Z., Garnavich, P. M., et al. 2006, *ApJL*, 645, L21
- Moldon, J., Horesh, A., Perez-Torres, M., Sfaradi, I., & Lundqvist, P. 2020, *ATel*, 13448, 1
- Nakamura, T., Mazzali, P. A., Nomoto, K., & Iwamoto, K. 2001, *ApJ*, 550, 991
- Nakar, E., & Piro, A. L. 2014, *ApJ*, 788, 193
- Nath, B. B., Laskar, T., & Shull, J. M. 2008, *ApJ*, 682, 1055
- Nozawa, T., Kozasa, T., Habe, A., et al. 2007, *ApJ*, 666, 955
- Nozawa, T., Kozasa, T., Tominaga, N., et al. 2008, *ApJ*, 684, 1343
- Nozawa, T., Kozasa, T., Umeda, H., Maeda, K., & Nomoto, K. 2003, *ApJ*, 598, 785
- Pastorello, A., Mattila, S., Zampieri, L., et al. 2008, *MNRAS*, 389, 113
- Patat, F., Cappellaro, E., Danziger, J., et al. 2001, *ApJ*, 555, 900
- Penney, R., & Hoefflich, P. 2014, *ApJ*, 795, 84
- Perley, D., Schulze, S., & Bruch, R. 2020, *TNSAN*, 37, 1
- Petuchowski, S. J., Dwek, E., Allen, J. E., & Nuth, J. 1989, *ApJ*, 342, 406, J. A., 1
- Piro, A. L. 2015, *ApJL*, 808, L51
- Poznanski, D., Prochaska, J. X., & Bloom, J. S. 2012, *MNRAS*, 426, 1465
- Rho, J., Geballe, T. R., Banerjee, D. P. K., et al. 2018a, *ApJL*, 864, L20
- Rho, J., Gomez, H. L., Boogert, A., et al. 2018b, *MNRAS*, 479, 5101
- Rho, J., Kozasa, T., Reach, W. T., et al. 2008, *ApJ*, 673, 271
- Rho, J., Onaka, T., Cami, J., & Reach, W. T. 2012, *ApJL*, 747, L6
- Sakon, I., Onaka, T., Wada, T., et al. 2009, *ApJ*, 692, 546
- Sarang, I., & Cherchneff, A. 2013, *ApJ*, 776, 107
- Sarang, I., & Cherchneff, A. 2015, *A&A*, 575, A95
- Sarang, I., Dwek, E., & Arendt, G. 2018, *ApJ*, 859, 66
- Sauer, D. N., Mazzali, P. A., Deng, J., et al. 2006, *MNRAS*, 369, 1939
- Schlafly, E. F., & Finkbeiner, D. P. 2011, *ApJ*, 737, 103
- Sharp, C. M., & Hoefflich, P. 1989, *HiA*, 8, 207
- Sharp, C. M., & Hoefflich, P. 1990, *Ap&SS*, 171, 213
- Shorridge, K., Meyerdirks, H., & Bridger, A. 1992, *StASN*, 40
- Siebert, M. R., Kilpatrick, C. D., Foley, R. J., & Cartier, R. 2020, *ATel*, 13393, 1
- Silvia, D. W., Smith, B. D., & Shull, J. M. 2010, *ApJ*, 715, 1575
- Sluder, A., Milosavljević, M., & Montgomery, M. H. 2018, *MNRAS*, 480, 5580
- Smith, N., & Ferland, G. J. 2007, *ApJ*, 655, 911
- Smith, N., Foley, R. J., Bloom, J. S., et al. 2008, *ApJ*, 686, 485
- Smith, N., Gehrz, R. D., Hinz, P. M., et al. 2003, *AJ*, 125, 1458
- Sollerman, J., Leibundgut, B., & Spyromilio, J. 1998, *A&A*, 337, 207
- Spyromilio, J., Meikle, W. P. S., Learner, R. C. M., & Allen, D. A. 1989, in Proc. of the 22nd Eslab Symp., Infrared Spectroscopy in Astronomy, ed. E. Böhm-Vitense (Noordwijk: European Space Agency), 381
- Stanek, K. Z. 2020, Transient Name Server Discovery Report, 2020-381, 1
- Stetson, P. B. 2000, *PASP*, 112, 925
- Stevance, H. F., Maund, J. R., Baade, D., et al. 2017, *MNRAS*, 469, 1897
- Stevance, H. F., Maund, J. R., Baade, D., et al. 2019, *MNRAS*, 485, 102
- Szalai, T., Vinkó, J., Könyves-Tóth, R., et al. 2019, *ApJ*, 876, 19
- Thomas, R. C., Nugent, P. E., & Meza, J. C. 2011, *PASP*, 123, 237
- Tielens, A. G. G. M. 2005, The Physics and Chemistry of the Interstellar Medium (Cambridge: Cambridge Univ. Press)
- Tinyanont, S., Kasliwal, M. M., Krafton, K., et al. 2019, *ApJ*, 873, 127
- Todini, P., & Ferrara, A. 2001, *MNRAS*, 325, 726
- Tody, D. 1986, *Proc. SPIE*, 627, 733
- Tody, D. 1993, in ASP Conf. Ser. 52, Astronomical Data Analysis Software and Systems II, ed. R. J. Hanisch, R. J. V. Brissenden, & J. Barnes (San Francisco, CA: ASP), 173
- Tonry, J. L., Stubbs, C. W., Lykke, K. R., et al. 2012, *ApJ*, 750, 99
- Vacca, W. D., Cushing, M. C., & Rayner, J. T. 2003, *PASP*, 115, 389
- Valenti, S., Elias-Rosa, N., Taubenberger, S., et al. 2008, *ApJL*, 673, L155
- Valenti, S., Howell, D. A., Stritzinger, M. D., et al. 2016, *MNRAS*, 459, 3939
- Valenti, S., Sand, D., Pastorello, A., et al. 2014, *MNRAS*, 438, L101
- Wang, C.-J., Bai, J.-M., Fan, Y.-F., et al. 2019, *RAA*, 19, 149
- Wang, L., Baade, D., Hoefflich, P., & Wheeler, J. C. 2003, *ApJ*, 592, 457
- Waxman, E., Mészáros, P., & Campana, S. 2007, *ApJ*, 667, 351
- Wheeler, J. C., Harkness, R. P., Barker, E. S., Cochran, A. L., & Wills, D. 1987, *ApJL*, 313, L69
- Williamson, M., Modjaz, M., & Bianco, F. B. 2019, *ApJL*, 880, L22
- Woosley, S., & Bloom, J. 2006, *ARA&A*, 44, 507
- Woosley, S. E., Eastman, R. G., & Schmidt, B. P. 1999, *ApJ*, 516, 788
- Xin, Y.-X., Bai, J.-M., Lun, B.-L., et al. 2020, *RAA*, 20, 9
- Yoon, S.-C. 2015, *PASA*, 32, 15
- Yoon, S.-C. 2017, *MNRAS*, 470, 3970
- Yoon, S.-C., Chun, W., Tolstov, A., Blinnikov, S., & Dessart, L. 2019, *ApJ*, 872, 174
- Zackay, B., & Ofek, E. O. 2017, *ApJ*, 836, 187